

EXPERIMENTAL INVESTIGATION OF VENTURI MICROBUBBLE GENERATION IN A VISCOSUS
FLUID USING TEMPERATURE-CONTROLLED FACILITY

By

Andrew Phillip Noonan

Thesis

Submitted to the Faculty of the
Graduate School of Vanderbilt University
in partial fulfillment of the requirements
for the degree of

MASTER OF SCIENCE

in

Mechanical Engineering

August 2025

Nashville, Tennessee

To-Be Approved:

Amrutar Anilkumar, Ph.D.

Kane Jennings, Ph.D.

Robert Pitz, Ph.D.

Copyright © 2025 Andrew Phillip Noonan
All Rights Reserved

ACKNOWLEDGMENTS

First, I would like to express my gratitude to Dr. Amrutar Anilkumar for his mentorship, guidance, and support over the past few years. His steady approach to science and engineering and dedication to his students have profoundly shaped both the engineer I am today and the professional I aspire to become. His ability to bring out the best in his students is truly remarkable.

I would also like to thank Dr. Robert Pitz and Dr. Kane Jennings for serving on my committee and for their valuable insight and feedback, which helped refine and strengthen this work.

To my family, Faye, Eric, and Danielle (and all my loving cousins/aunts/uncles) thank you for your unconditional love and support throughout this journey. I would not be where or who I am without you, and I could not be more grateful.

To my friends from both undergrad and grad school at Vanderbilt, thank you for making this time in my life so meaningful and unforgettable. And to my friends back home, your constant support and sense of humor have carried me through everything, thank you.

I would also like to thank Mark Dalton, whose generous donations establishing the Mark Dalton Vanderbilt Aerospace Design Laboratory fund have enabled this work at Vanderbilt.

TABLE OF CONTENTS

	Page
LIST OF TABLES	vi
LIST OF FIGURES	vii
1 Introduction	1
1.1 Background	1
1.2 Venturi-Based Fragmentation Mechanism	1
1.3 Fluid Selection and Properties	3
2 Facility Description and Experimental Method	6
2.1 Experimental Setup and Facility	6
2.2 Venturi Generator Design and Fabrication	8
2.3 Imaging Setup	9
2.4 Timing Diagram for Imaging	11
2.5 Summary of Aeration Experiments	12
2.6 Image and Data Processing	13
3 Results of Aeration Experiments	15
3.1 Qualitative Observations of Bubble Fragmentation	15
3.2 Analysis of Bubble Size Distribution	15
3.3 Effect of Flow Rate	20
3.4 Effect of Diverging Angle	22
3.5 Effect of Temperature (Viscosity and Surface Tension)	23
4 Empirical Analysis	25
4.1 Reynolds Number Investigation	25
4.2 Capillary Number Investigation	27
4.3 Weber Number Investigation	28
4.4 Universality Investigation	29
5 Discussion	31
References	32
APPENDIX	34
A Facility Information	35
A.1 LabVIEW Interface	35
A.2 Data Acquisition and Control Circuit	36

A.3	Temperature Calibration	38
A.4	Timing Calculations	39
A.5	Imaging Depth of Field	40
A.6	Speed of Sound in Two-Phase Medium	41
A.7	Operational Safety	41
B	Supplementary Plots and Data	43
B.1	Effect of Flow Rate Supplementary Plots	43
B.2	Effect of Diverging Angle Supplementary Plots	43
B.3	Effect of Temperature Supplementary Plots	45

LIST OF TABLES

Table	Page
1.1 Summary of 50 cSt fluid properties for experimental conditions.	5

LIST OF FIGURES

Figure	Page
1.1 Schematic of Venturi bubble generator illustrating key geometry and flow variables.	1
1.2 Illustration demonstrating the increased surface tension energy in fragmented bubbles.	2
1.3 50 cSt PMX-200 Series density and viscosity vs temperature from Roberts et al. (2017).	4
2.1 Experimental facility overview.	6
2.2 Experimental facility schematic.	7
2.3 Air injection system built for the present study.	8
2.4 Cross section view of Venturi design features and key variables (7° shown here).	9
2.5 Flow visualization and imaging cell.	10
2.6 Imaging plug insert, measurement, and sample image.	11
2.7 Segment lengths and diameters for volume/flow time estimation.	11
2.8 Image timing diagrams for 1.5 and 5.5 GPM trials.	12
2.9 Temperature vs time for a typical aeration experiment (shown at $120^\circ F$, 4.5 GPM, 15° , trial 1).	13
2.10 Image processing for bubble characterization.	14
3.1 Straight pipe vs 15° comparison at 5.5 GPM, $\alpha = 0.2\%$, $225^\circ F$	15
3.2 1.5 GPM vs 5.5 GPM and $120^\circ F$ vs $225^\circ F$ sample image comparison for $\beta = 15^\circ$, $\alpha = 0.2\%$	16
3.3 Bubble size distribution for 7° half-angle, $225^\circ F$, $\alpha = 0.2\%$	17
3.4 Probability density function for 7° half-angle, $225^\circ F$, $\alpha = 0.2\%$ in log (a) and normal (b) scales.	18
3.5 Probability density function for 7° half-angle, $225^\circ F$, $\alpha = 0.2\%$ in log (a) and normal (b) scales with d_{30} and d_{32} labeled.	19
3.6 R^2 value between trial 1 and trial 2 statistical values derived from image processing for all temperatures, diverging half-angles, and flow rates at 0.2% aeration.	20
3.7 Probability density functions for all flow rates at $\beta = 15^\circ$, $225^\circ F$, $\alpha = 0.2\%$	21
3.8 Effect of flow rate on bubble diameter, $\beta = 15^\circ$, $\alpha = 0.2\%$	21
3.9 PDF distributions for all angles 5.5 GPM, $225^\circ F$, $\alpha = 0.2\%$	22
3.10 Effect of Venturi angle β on bubble characteristics at 5.5 GPM, $\alpha = 0.2\%$	23
3.11 DOW PMX-200 Series Variation of Surface Tension and Viscosity with Temperature.	23
3.12 Effect of temperature on bubble characteristics, $\beta = 15^\circ$, $\alpha = 0.2\%$	24
4.1 d_{30}/D_t vs Reynolds for present study at 15° Venturi angle.	26
4.2 d_{30}/D_t vs Reynolds for present study and Yin et al. (2015); Sun et al. (2017).	26
4.3 d_{30}/D_t vs Capillary for present study at 15° Venturi angle.	27
4.4 d_{30}/D_t vs Capillary for present study and Yin et al. (2015); Sun et al. (2017).	28
4.5 d_{30}/D_t vs Weber for present study at 15° Venturi angle.	28
4.6 d_{30}/D_t vs Weber for present study and Yin et al. (2015); Sun et al. (2017).	29
4.7 d_{30}/D_t vs $Re^a \cdot We^b$ fit including (a) and excluding external data from (b) Yin et al. (2015); Sun et al. (2017).	29
4.8 d_{30}/D_t vs $Re^c \cdot Ca^d$ fit including (a) and excluding external data from (b) Yin et al. (2015); Sun et al. (2017).	30
A.1 LabVIEW Graphical User Interface for measurement, data logging, and facility control.	35
A.2 LabVIEW back panel for measurement, data logging, and facility control.	36
A.3 Designed data acquisition and control circuitry.	37
A.4 Data acquisition and control circuit.	38
A.5 Pt100 calibration data against Hg and digital thermometers.	39
A.6 Image timing diagram for 2.5 GPM trials.	39
A.7 Image timing diagram for 3.5 GPM trials.	40

A.8	Image timing diagram for 4.5 GPM trials.	40
A.9	Camera setup for depth of field measurement.	41
B.1	Effect of flow rate on bubble diameter, $\beta = 7^\circ$, $\alpha = 0, 2\%$	43
B.2	Effect of flow rate on bubble diameter, $\beta = 30^\circ$, $\alpha = 0, 2\%$	43
B.3	Effect of Venturi angle β on bubble characteristics at 1.5 GPM, $\alpha = 0.2\%$	44
B.4	Effect of Venturi angle β on bubble characteristics at 2.5 GPM, $\alpha = 0.2\%$	44
B.5	Effect of Venturi angle β on bubble characteristics at 3.5 GPM, $\alpha = 0.2\%$	45
B.6	Effect of Venturi angle β on bubble characteristics at 4.5 GPM, $\alpha = 0.2\%$	45
B.7	Effect of temperature on bubble characteristics, $\beta = 7^\circ$, $\alpha = 0.2\%$	46
B.8	Effect of temperature on bubble characteristics, $\beta = 30^\circ$, $\alpha = 0.2\%$	46

CHAPTER 1

Introduction

1.1 Background

Aerated liquids find wide engineering applications in nuclear, water treatment, chemical, pharmaceutical, and food processing industries. Microbubble suspensions enhance liquid-gas processes due to large surface area to volume ratios and long residence times in liquids. In flow-based aeration, in-line Venturi devices achieve high aeration in simple, energy efficient, and reliable way. Flow-based helium bubble injection via Venturi bubble generators into molten fuel salt (7LiF-BeF₂-UF₄) is used to remove gaseous fission products from nuclear fuels (Gabbard, 1972; Robertson et al., 1970; Li et al., 2017). Venturi-generated microbubbles play an integral role in water treatment, facilitating oxygenation, contaminant flotation, and sterilization (Agarwal et al., 2011; Budhijanto et al., 2017; Terasaka et al., 2011). In the chemical and food processing industries, Venturi microbubble generators are used for removing biofilm and pesticides, hydroponic farming, and food texture modification (Bhat et al., 2025; Lu et al., 2023; Sharma et al., 2005). The majority of scientific studies in Venturi-based aeration are limited to air–water systems. The current experimental investigation expands the landscape by examining the role of fluid viscosity and surface tension in bubble fragmentation using a homogeneous and viscous working silicone oil operated at various controlled temperatures.

1.2 Venturi-Based Fragmentation Mechanism

Figure 1.1 shows the injection of air into flowing fluid in the Venturi throat. As the injected bubbles travel through the diverging section, they are fragmented by intense shear in the recirculating region. The focus of this experimental study is to examine the role of fluid viscosity μ and surface tension σ in bubble fragmentation.

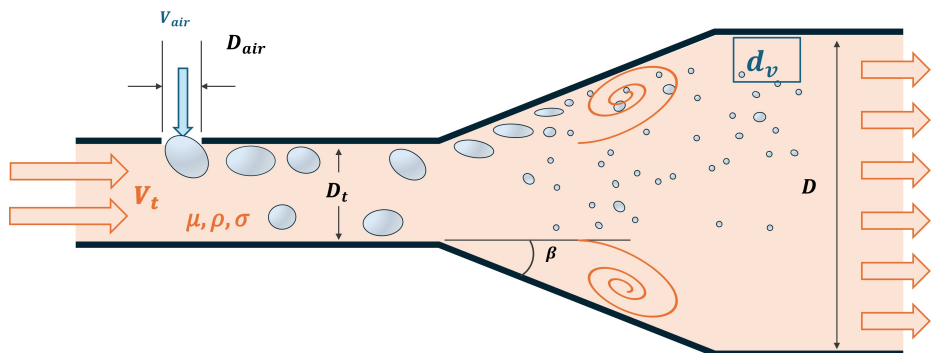


Figure 1.1: Schematic of Venturi bubble generator illustrating key geometry and flow variables.

The nature of the shear-based bubble breakup mechanism in subsonic two-phase flow has been studied by several investigators (Hinze, 1955; Zhao et al., 2019, 2024; Nomura et al., 2011). Hinze (1955) developed a theoretical framework to understand bubble breakup using dimensionless groups, primarily the Weber number which represents the role of flow energy $\frac{\rho V^2 D}{\sigma}$ and Ohnesorge number representing viscous shear $\frac{\mu}{\sqrt{\rho \sigma D}}$.

Consequent to the nature of the two-phase flow in the Venturi, the effective acoustic velocity will be lower than that of the constituent liquid and gaseous phases, and therefore the flow can potentially become supersonic in the diverging section. In the latter context, the mechanism for bubble fragmentation would differ from subsonic flow (Nomura et al., 2011). In the current experimental investigation, the speed of the two-phase flow does not exceed the speed of sound at the throat (Calculation in Appendix A.6).

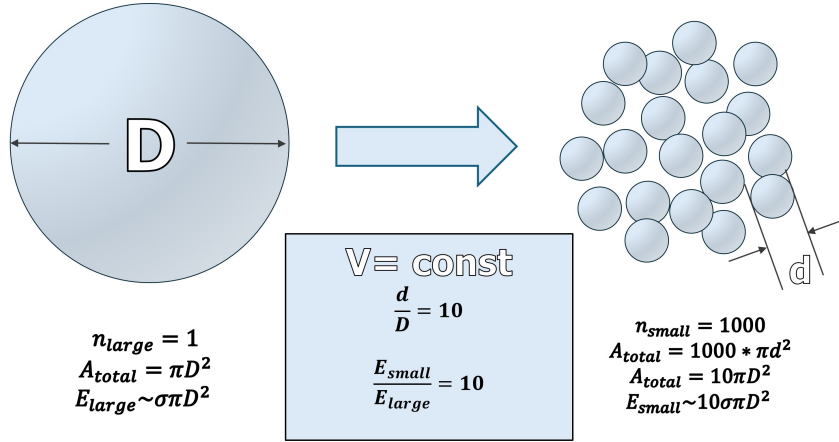


Figure 1.2: Illustration demonstrating the increased surface tension energy in fragmented bubbles.

Figure 1.2 schematically illustrates the energy cost of fragmentation; breaking a single large bubble (left) into many smaller ones (right) increases the surface energy. This energy to sustain the dispersed state must come from the flow, and the efficiency of converting flow energy to surface energy has been analyzed by Murai et al. (2021).

A simplified understanding of bubble fragmentation can be developed using a nondimensional framework. The representative bubble diameter d_b is a function of fluid physical properties, Venturi geometric design, and flow operational parameters:

$$d_b = f(V_t, \rho, \mu, \sigma, D_t, V_{air}, \beta, D, D_{air}) \quad (1.1)$$

V_t is the throat velocity, μ, ρ , and σ are the liquid phase dynamic viscosity, density, and surface tension respectively. D is the entry/exit diameter, D_t is the Venturi throat diameter, D_{air} is the Venturi air inlet diameter, V_{air} is the air inlet velocity, and β is the diverging half-angle (see Figure 1.1 for reference).

In dimensional analysis, D_t is selected as the characteristic length scale, as the air inlet diameter D_{air} has been shown to have negligible influence on final bubble size by Li et al. (2017). For a given geometry of the

Venturi and a fixed injection rate, Equation 1.1 simplifies to:

$$d_b = f(V_t, \rho, \mu, \sigma, D_t) \quad (1.2)$$

If ρ, V_t , and D_t are chosen as the repeating variables, the following three nondimensional terms are formed

$$\frac{d_b}{D_t} = \phi \left(\frac{\rho V_t D_t}{\mu}, \frac{\rho V_t^2 D_t}{\sigma} \right) = \phi (Re, We) \quad (1.3)$$

If μ, V_t , and D_t are chosen as the repeating variables, the following three nondimensional terms are formed

$$\frac{d_b}{D_t} = \phi \left(\frac{\rho V_t D_t}{\mu}, \frac{\mu V_t}{\sigma} \right) = \phi (Re, Ca) \quad (1.4)$$

The Reynolds number is present in both the nondimensional groupings indicating the flow condition in the throat, while the dependence on the Weber or the Capillary number is examined in the present investigation. In prior work, Gabbard (1972) utilized Reynolds and the Ohnesorge-related grouping $\frac{\sigma \rho D_t}{\mu^2}$ which is a product of Weber and Capillary numbers to examine bubble fragmentation, but the studies were incomplete due to inadequate experimental data. The Ohnesorge number is related to Weber and Capillary numbers as follows:

$$\frac{1}{Oh^2} \equiv \frac{\sigma \rho D_t}{\mu^2} = \left(\frac{\rho V_t^2 D_t}{\sigma} \right) \left(\frac{\sigma}{\mu V_t^2} \right) = \frac{We}{Ca^2} \quad (1.5)$$

In this temperature-controlled experimental with a single fluid, the relevance of Reynolds, Weber and Capillary numbers will all be independently examined in their capability to predict $\frac{d_b}{D_t}$. Existing experimental studies on Venturi bubble fragmentation have predominantly used water-air systems. Murai et al. (2021) and Gabbard (1972) have varied the operating viscosity by using water-glycerin mixtures and $CaCl_2$ aqueous solution in a small range up to 4 cP. Surfactants were also used to lower surface tension by Gabbard (1972), but authors noted that inhomogeneity in surfactant distribution in the working fluid led to poor repeatability, leaving surface tension effects largely unexplored. No prior work robustly investigates bubble fragmentation under controlled variation of both viscosity and surface tension in a single fluid. The use of a homogeneous, viscous working fluid at various well-controlled temperatures avoids local variation of properties due to inadequate mixing or use of surfactants.

1.3 Fluid Selection and Properties

The objective of this study is to investigate the effects of viscosity and surface tension on bubble formation in Venturi injectors using a temperature-controlled working fluid. In the present study, 50 cSt polydimethylsilox-

ane (PDMS) from the Dow PMX-200 series was chosen for its well-characterized thermophysical properties (Roberts et al., 2017), optical clarity, and non-volatility. This fluid allowed systematic variation of viscosity and surface tension by altering the fluid temperature. Three set temperature points were used in experiments: 120°F, 180°F, and 225°F. These correspond to the low, mid, and high ends of the operating temperature range of the experimental facility. A summary of density and viscosity across this range is shown in Table 1.1 and plotted in Figure 1.3.

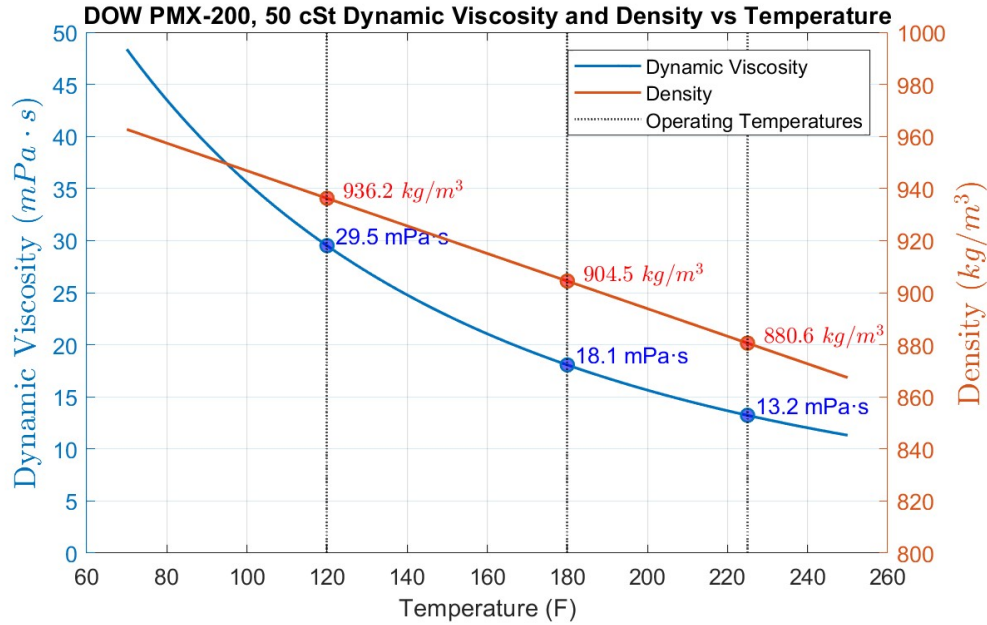


Figure 1.3: 50 cSt PMX-200 Series density and viscosity vs temperature from Roberts et al. (2017).

Viscosity data was obtained from the Sandia National Laboratories report on 50cSt PDMS thermal properties (Roberts et al., 2017). Viscosity decreases nonlinearly with temperature with an equation of the form

$$\log_{10} \mu = \frac{732}{T} - 3.802 \quad (1.6)$$

where μ is the viscosity in $\text{Pa} \cdot \text{s}$, T is the temperature in Kelvin. At 120°F, the dynamic viscosity is 29.5 $\text{mPa} \cdot \text{s}$, while at 225°F, it decreases to 13.2 $\text{mPa} \cdot \text{s}$. The temperature in the experimental facility is controlled to $\pm 1^\circ$, and the viscosity is accurate to within 1%.

Density data was also determined from the Sandia report. PDMS density decreases linearly with temperature, from approximately $936.2 \frac{\text{kg}}{\text{m}^3}$ at 120°F to $880.6 \frac{\text{kg}}{\text{m}^3}$ at 225°F. This corresponds to a decrease of 5.9%.

Surface tension data is referenced from Darhuber et al. (2003). While specific data for the surface tension temperature dependence of 50 cSt PDMS is unavailable, the relationship for 20 cSt PDMS fluid from 0 –

100°C, yields a linear temperature coefficient of $-0.06 \frac{mN}{mK}$ and has been used for this fluid of the same series.

In the Dow PMX-200 series fluids, surface tension is largely independent of viscosity grade, with 20 cSt, 50 cSt, and 100 cSt PDMS fluids having surface tensions of 20.6 $\frac{mN}{m}$, 20.8 $\frac{mN}{m}$, and 20.9 $\frac{mN}{m}$ respectively at 25°C (DowChemicalCompany, 2017, 2024). It is therefore reasonable to assume that the 50 cSt fluid possesses the same temperature coefficient of $-0.06 \frac{mN}{mK}$, yielding the following equation, where σ is surface tension in $\frac{mN}{m}$, and T is temperature in Celsius.

$$\sigma = 22.3 - 0.06T \frac{mN}{m} \quad (1.7)$$

Surface tension of 50 cSt PDMS decreases by about 18% across the tested temperature range from 19.4 $\frac{mN}{m}$ at 120°F to 15.9 $\frac{mN}{m}$ at 225°F. All working fluid properties are summarized in Table 1.1 and have been incorporated during evaluation of the temperature-controlled experimental data.

Temperature (°F)	μ (mPa·s)	σ (mN/m)	ρ (kg/m ³)	ν (cSt)
72	47.3	21.0	961.6	49.2
120	29.5	19.4	936.2	31.5
180	18.1	17.4	904.5	20.0
225	13.2	15.9	880.6	15.0

Table 1.1: Summary of 50 cSt fluid properties for experimental conditions.

CHAPTER 2

Facility Description and Experimental Method

2.1 Experimental Setup and Facility

The experimental facility used in this study is shown in Figure 2.1, with a detailed schematic provided in Figure 2.2. This setup is based on an earlier design (Smith and Anilkumar, 2022) which was subsequently modified by Schepner et al. (2023) for testing oil filter friction factors and evaluating lubricant oil health for diesel engine applications. Prior to the current experiments, this facility was repeatedly flushed out with DOW PMX-200 Series flushing fluid before using a fresh working fluid. The facility's key components include a gear pump, large surface area heater, oil filter, reservoir tank, and temperature and pressure sensors. This temperature-controlled facility with precise flow rate control was modified to include a Venturi microbubble generator (Section 2.2) and air injection system to conduct the present studies.

Figure 2.1 shows the experimental facility with color-coded lines representing key flow regions: post-pump/pre-filter, post-filter/pre-pump, and the Venturi and flow visualization section.

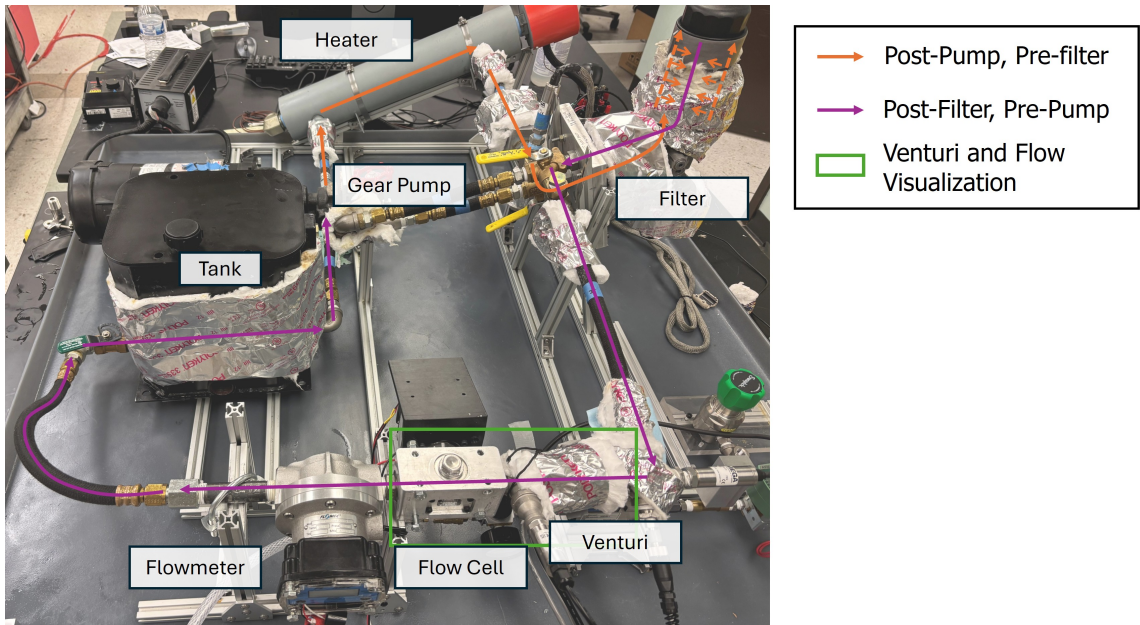


Figure 2.1: Experimental facility overview.

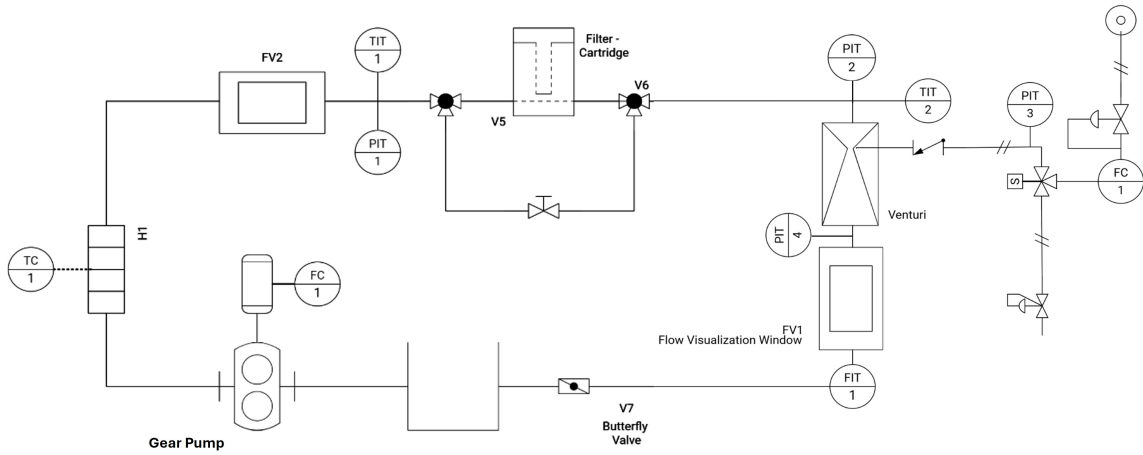


Figure 2.2: Experimental facility schematic.

Oil flow is driven by the rotary gear pump (Dayton 4KHC7) coupled to a DC permanent magnet motor (Dayton 2M170). For this study, the fluid working temperatures were in the range $120^{\circ}F - 225^{\circ}F$, and the flow rates were between $1.5 - 5.5$ GPM. The flow rate was monitored using an oval gear flow meter (Flomec OM Series) (Figure 2.2, FIT1) designed for high temperature applications, providing high accuracy (0.5%) in the viscosity regime of interest.

Air is injected under positive pressure at the Venturi throat with a check valve to prevent backflow of oil into the air system. The air injection system (Figure 2.3) begins with shop air regulated down to 25 psi. Air flow is managed by a Omega mass flow controller (FMA6500) (Figure 2.2, FC1), and is operated from $10 - 100 \frac{mL}{min}$ with $\pm 2 \frac{mL}{min}$ accuracy. Before the start of air injection and to accommodate the flowmeter warm-up period (~ 15 minutes), a computer-controlled solenoid valve initially diverts air to the ambient before switching to injection mode.

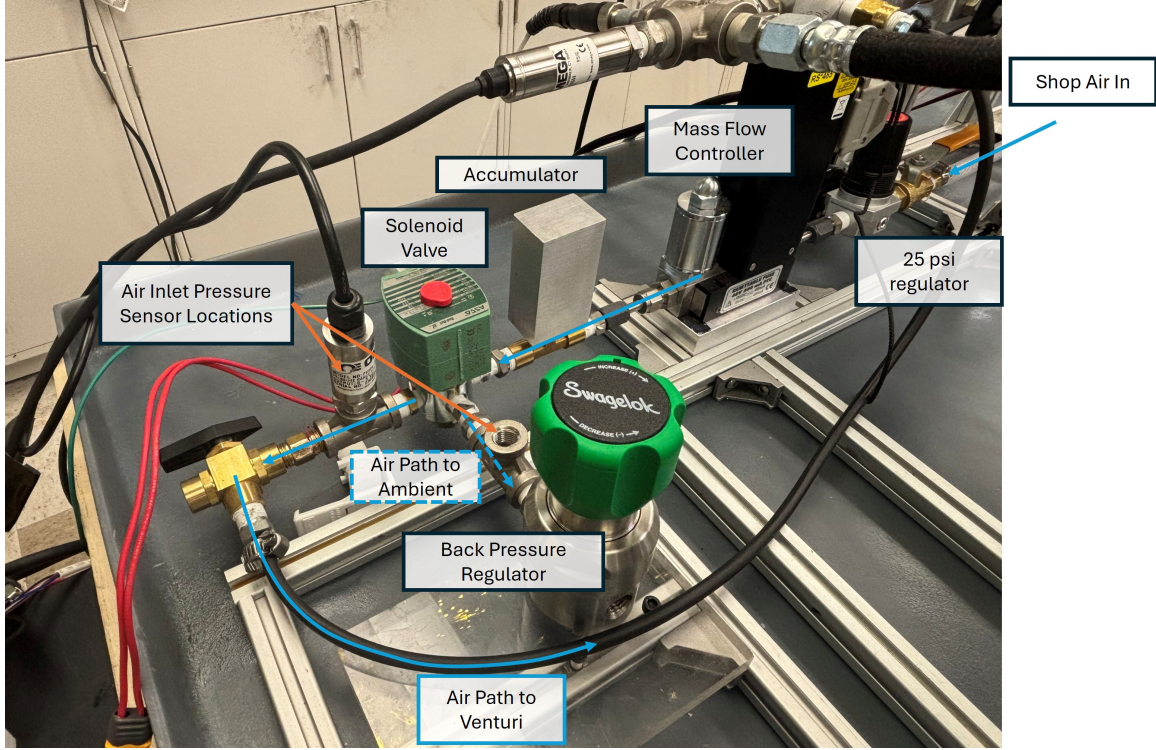


Figure 2.3: Air injection system built for the present study.

Heating of the working oil is accomplished by a Watlow large surface area submersible heater in conjunction with a Tempco 15A controller. The heater's low power density enables stable temperature control while avoiding local hot spots. The controller allows temperature setpoints in $1^{\circ}F$ increments. In this study, fluid temperature is measured just before the Venturi entrance (Figure 2.2, TIT2) using a Pt100 RTD (Omega RTD). The Venturi nozzle is insulated with $\frac{1}{2}$ -inch fiberglass batting. Details on temperature calibration and control circuitry are provided in Appendix A, and additional safety information is provided in Appendix A.7. Pressure measurements are taken immediately upstream and downstream of the Venturi (Figure 2.2, PIT2, PIT4) using Omega PX409 with $\pm 0.08\%$ accuracy. The upstream transducer has a working range of 0–50 *psi*, while the downstream unit has a working range 0–15 *psi*, suitable for making in-line measurements under all working conditions.

2.2 Venturi Generator Design and Fabrication

Three Venturi microbubble generators with diverging half-angles (β) of 7° , 15° , and 30° were designed for this study, each with consistent throat size and symmetric entry and exit geometry. Figure 2.4 shows a labeled schematic of a typical Venturi nozzle, with key design features summarized below:

- Entry half-angle (θ): 15°

- Throat diameter (D_t): 6 mm
- Inlet/outlet pipe diameter (D): 15.8 mm, diameter ratio $D_t/D = 0.38$
- Air injection hole diameter (d_{air}): 1 mm
- Process connections: $\frac{1}{2}$ – 14 NPT
- Diverging half-angle (β): 7°

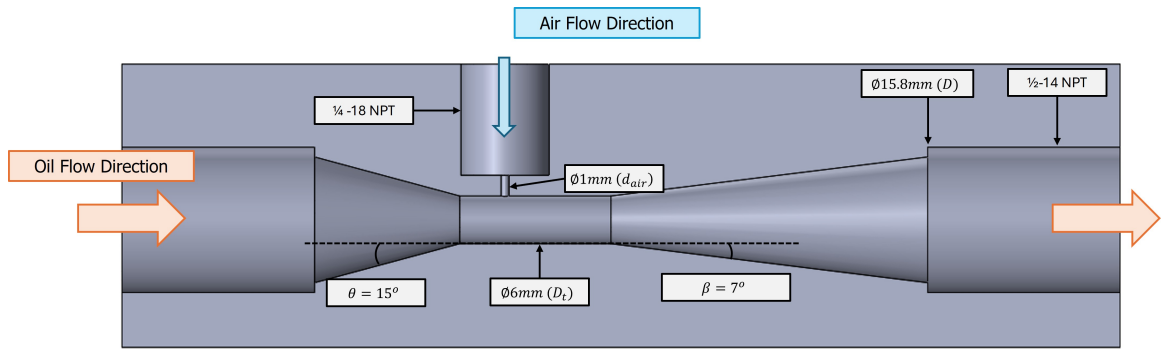


Figure 2.4: Cross section view of Venturi design features and key variables (7° shown here).

The diverging half-angle, β , establishes the expansion length downstream of the throat and influences the local deceleration rate and bubble breakup behavior.

All Venturi microbubble generators were CNC machined in-house from 6061 aluminum, ensuring chemical compatibility with Dow PMX-200 working fluid and structural integrity at working temperatures and pressures. All nozzles were machined using tapered flat end mills with diameters within a ± 0.002 " tolerance. The 1.0 mm air injection port was drilled and centered precisely along the flow axis. $\frac{1}{2}$ – 14 NPT threads were tapped on both ends for integration into the liquid flow line, while $\frac{1}{4}$ – 18 NPT threads were tapped into the air injection port for locating a check valve.

A custom flow-visualization cell was designed and placed immediately downstream of the nozzle diverging section to image freshly formed bubbles. To establish that bubble fragmentation only occurs due to the nozzle geometry, a control straight pipe with air injection was flow-tested and verified under identical aeration conditions. Results for this test are shown in Section 3.1.

2.3 Imaging Setup

The imaging cell is directly downstream of the Venturi generator and is connected via a short, straight transition segment as shown in Figure 2.5a. This segment was included for mounting the downstream pressure sensor. Control tests using a straight-pipe nozzle with identical downstream geometry confirmed that bubble

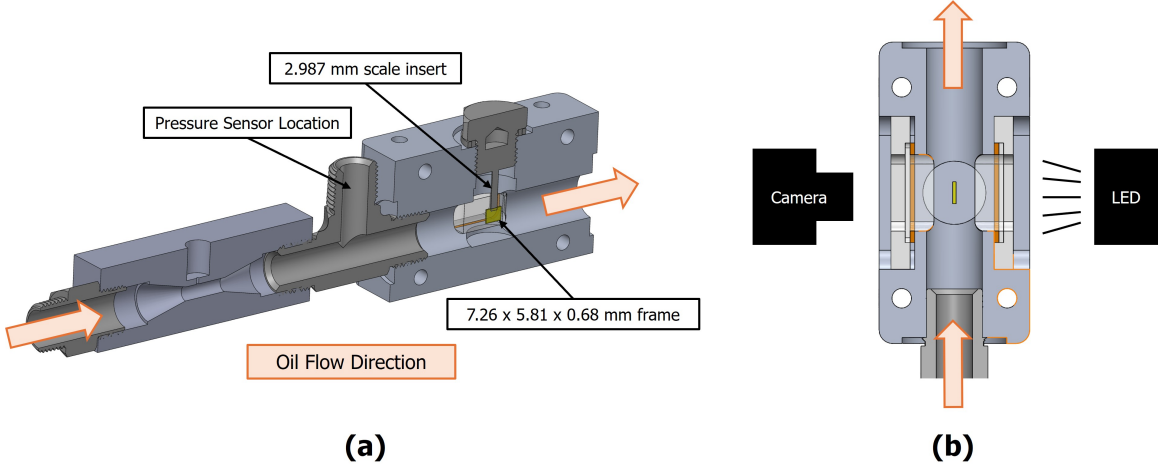


Figure 2.5: Flow visualization and imaging cell.

breakup occurs primarily in the diverging section of the nozzle and not in the intermediate region prior to imaging. Image comparison will be shown in the qualitative results section (3.1).

A 1280x1024 Chronos 1.4 high speed camera operating at 1000 frames per second (fps) with a $2 \mu\text{s}$ shutter speed was used to capture images downstream of the Venturi nozzle using a custom-built 100W LED light source (Figure 2.5b). The camera features a 55 mm f/2.8 Nikkor macro lens paired with a $2 \times$ teleconverter, resulting in an effective focal length of 110 mm at f/5.6. This configuration provided a clear field of view of 7.26×5.81 mm with a measured depth of field of 0.68 mm as shown in Figure 2.5a. Depth of field measurement and calculation is located in Appendix A.5.

A precision-machined plug with a known diameter of 2.987 mm was inserted into the flow visualization cell to provide real-time scaling. This plug was centered in the focal plane and used to determine pixel-to-length conversion ($5.87 \mu\text{m}/\text{pix}$), ensuring accurate size measurements without needing to correct for optical distortion through the Dow PMX-200 oil. Only bubbles appearing in focus were considered in the analysis. The plug, measurement, and a sample image are shown in Figure 2.6.



Figure 2.6: Imaging plug insert, measurement, and sample image.

2.4 Timing Diagram for Imaging

To ensure that recorded images capture freshly aerated flow, a timing analysis was conducted to estimate the oil loop travel time from the imaging section back to the Venturi nozzle.

Figure 2.7 shows the experiment facility with segment lengths and pipe sizes. Pipe lengths and diameters were measured to conservatively estimate segment volumes, and flow rates were used to calculate the total loop travel time. This results in a total volume of approximately 24.8 in^3 .

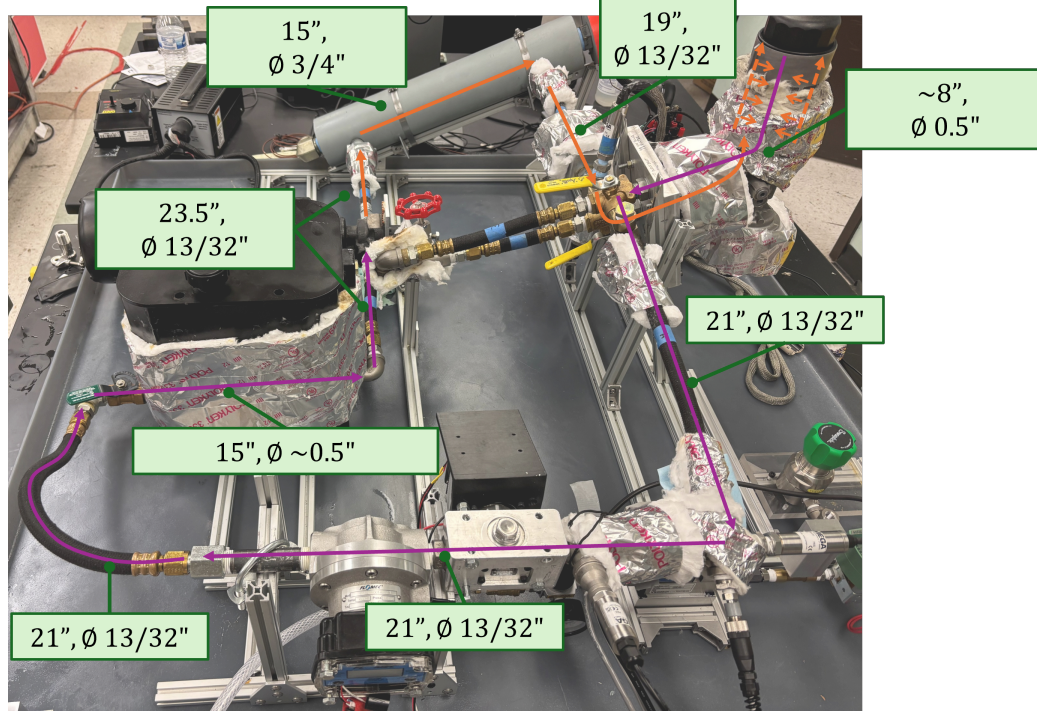


Figure 2.7: Segment lengths and diameters for volume/flow time estimation.

Timing diagrams (Figure 2.8a and Figure 2.8b) were created for the lowest and highest tested flow rates,

1.5 and 5.5 GPM. The gray bar indicates the loop travel time, while the blue bar shows the duration of the high-speed video capture window, which is 1.5 s (1500 frames) in the 1.5 GPM case, and 1.0s (1000 frames) for all other flow rates. For all flow rates, fifty image frames have been selected for measurement. For the 1.5 GPM case, every 29 frames are sampled, and the imaging time is approximately 1.45 seconds (gold bar) following the onset of air injection. At 1.5 GPM, the full loop recirculation time is 4.30 seconds; 1.45 s of imaging ends well before bubbles complete one full loop. At 5.5 GPM, the loop time is 1.17 seconds, and sampling are taken every 8 frames for a total of 0.40 s required for image collection.

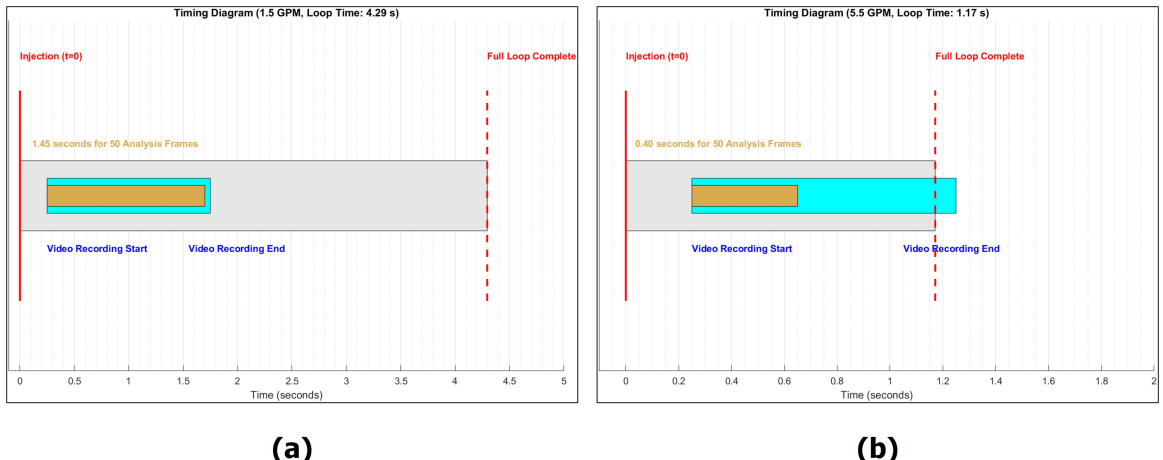


Figure 2.8: Image timing diagrams for 1.5 and 5.5 GPM trials.

This approach confirms that all measured bubbles were formed during initial pass-through of the Venturi nozzle and are not influenced by any residual or recycled air content. Further timing diagrams for other flow rates are found in Appendix A.4.

2.5 Summary of Aeration Experiments

Experiments were conducted using three Venturi nozzles with diverging half-angles of 7°, 15°, and 30° with constant throat diameter (D_t), inlet/outlet diameter (D), air injection port (D_{air}), and entry angle (θ). Three fluid temperatures (120°F, 180°F, and 225°F) and five flow rates (1.5, 2.5, 3.5, 4.5, and 5.5 GPM) were deployed in these studies. Two aeration levels of 0.2% and 0.5% by volume were used.

High-speed video was captured for each experiment to analyze freshly aerated flow. Fluid flow temperature was recorded during each study and the average value was used to determine fluid properties. Figure 2.9 shows a typical temperature profile for a 120°F trial at 4.5 GPM. Across all 90 experiments, the average temperature fluctuation was 0.6°F. At 120°F, where viscosity is most sensitive to temperature, these variations correspond to a maximum uncertainty of 1%.

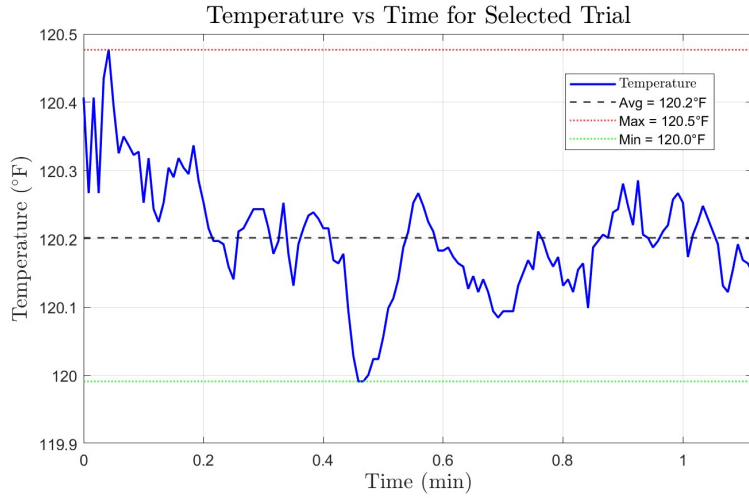


Figure 2.9: Temperature vs time for a typical aeration experiment (shown at 120°F, 4.5 GPM, 15°, trial 1).

2.6 Image and Data Processing

Sensor data including temperature, pressure (pre- and post-Venturi), liquid flow rate, air injection rate, and solenoid valve state were recorded using LabVIEW aligned with the imaging data. All video and sensor data were processed using a custom MATLAB-based image analysis suite developed with the Image Processing Toolbox (Mathworks, 2025). The approach was similar to that used in other studies (Yin et al., 2015; Gordiy-chuk et al., 2016; Sun et al., 2017) and was designed to ensure consistent and accurate bubble detection while minimizing user bias. An overview of the process is shown in Figure 2.10 and summarized in the following section.

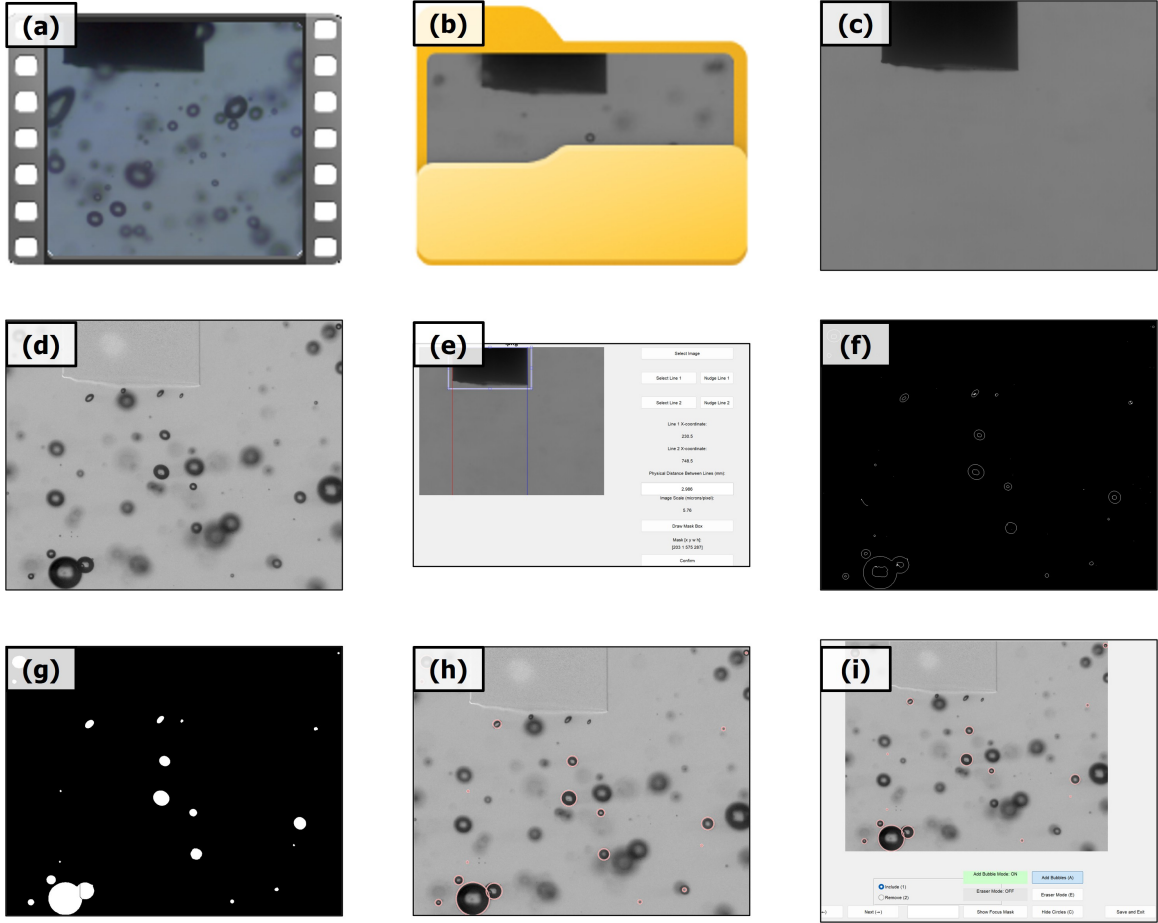


Figure 2.10: Image processing for bubble characterization.

After determining the required sample rate, black and white frames were exported from the high-speed videos (Figure 2.10a, 2.10b). A median image (Figure 2.10c) was generated from the set and subsequently subtracted from each frame (Figure 2.10d) to remove lighting non-uniformities and improve bubble contrast. The median image was also used for scale calibration using the precision-machined 2.987 mm plug visible in each frame (Figure 2.10e). A mask was applied to exclude regions near the plug where distortion or partial occlusions might affect bubble detection. Canny edge detection (Figure 2.10f) was used to find bubble outlines, followed by closing of small gaps and deletion of other artifacts. The enclosed regions were filled, and a watershed segmentation was applied to separate overlapping or touching bubbles (Figure 2.10g). A circular Hough transform (Figure 2.10h) was used to fit circles to the segmented regions and extract bubble properties such as diameter, centroid location, and area. Each frame was then manually reviewed using a custom interface (Figure 2.10i) to correct segmentation errors, remove out-of-focus bubbles, and verify accurate detection.

CHAPTER 3

Results of Aeration Experiments

3.1 Qualitative Observations of Bubble Fragmentation

Bubble fragmentation was qualitatively assessed across variations in flow rate, diverging angle, and fluid viscosity. Comparison between the presence of a diverging section and the absence of it (straight-pipe control) is shown in Figure 3.1 for the highest flow rate and temperature condition. This establishes that the presence of a diverging section is critical to effective bubble fragmentation.

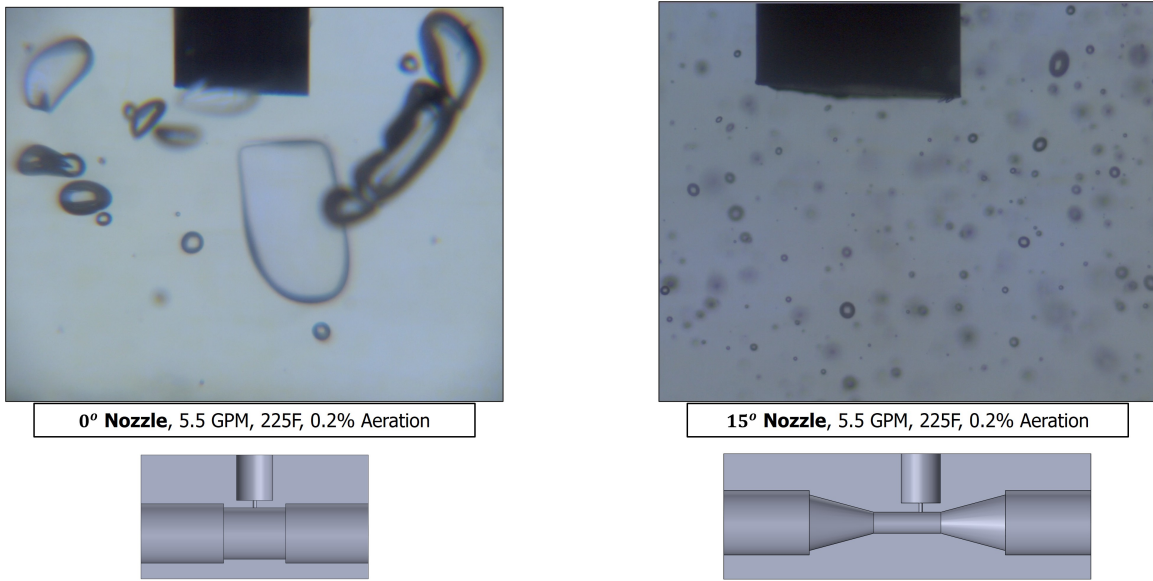


Figure 3.1: Straight pipe vs 15° comparison at 5.5 GPM, $\alpha = 0.2\%$, $225^\circ F$.

After ascertaining that the Venturi geometry is the primary driver of breakup, various flow rate and temperature combinations were examined for the 15° nozzle (Figure 3.2). For constant geometry, temperature, and aeration percentage, increasing the liquid flow rate from 1.5 to 5.5 GPM (Figure 3.2 a/c,b/d) produces smaller bubbles, consistent with increased flow energy as a driver for shear-induced bubble fragmentation. For a fixed flow rate, comparing high- and low-temperature fluid flows (Figure 3.2 a/b, c/d) shows that high-temperature fluid flow correlates with smaller bubble sizes, attributable to reduced viscosity and reduced surface tension.

3.2 Analysis of Bubble Size Distribution

For each experiment run, a set of fifty manually reviewed frames was used to generate a distribution of bubble sizes shown in Figure 3.3 for the 7° half-angle Venturi, with the working fluid operating at $225^\circ F$, 5.5 GPM

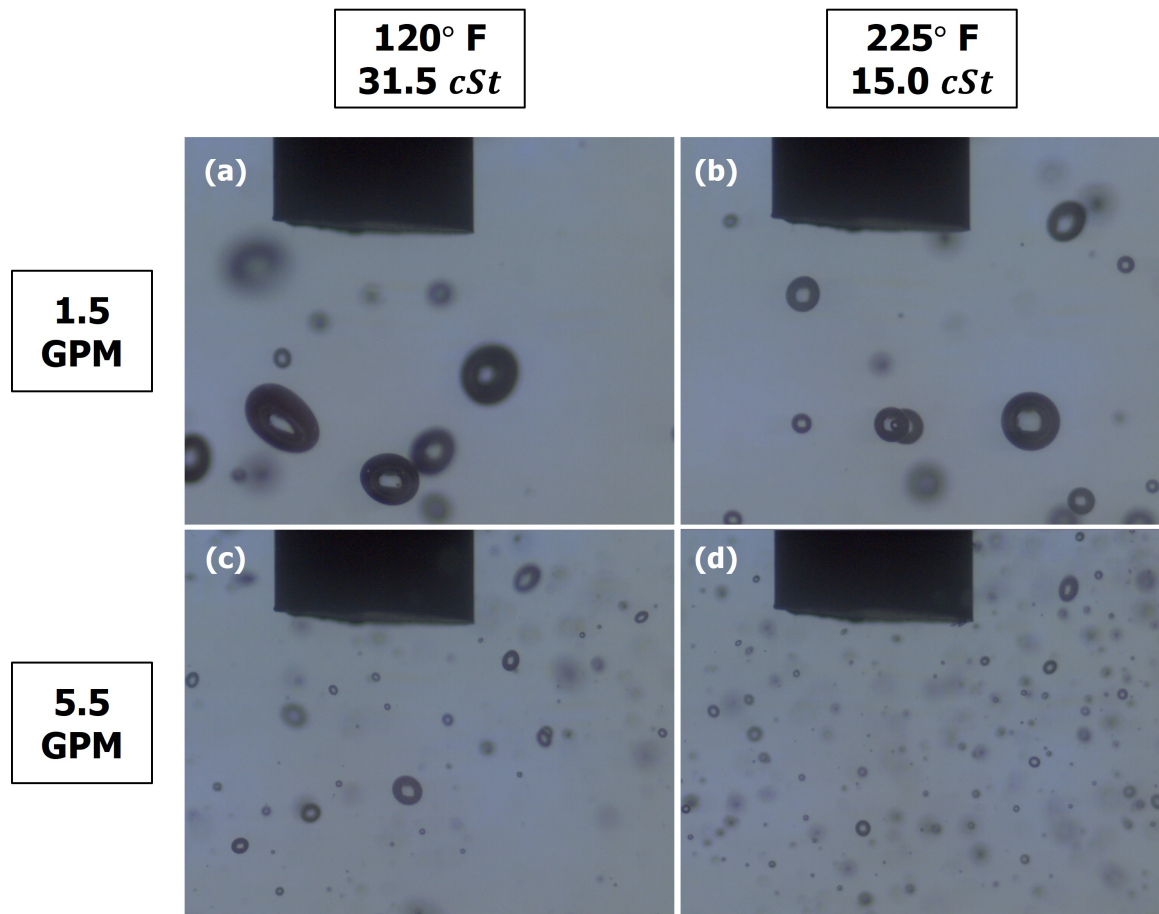


Figure 3.2: 1.5 GPM vs 5.5 GPM and 120°F vs 225°F sample image comparison for $\beta = 15^\circ$, $\alpha = 0.2\%$.

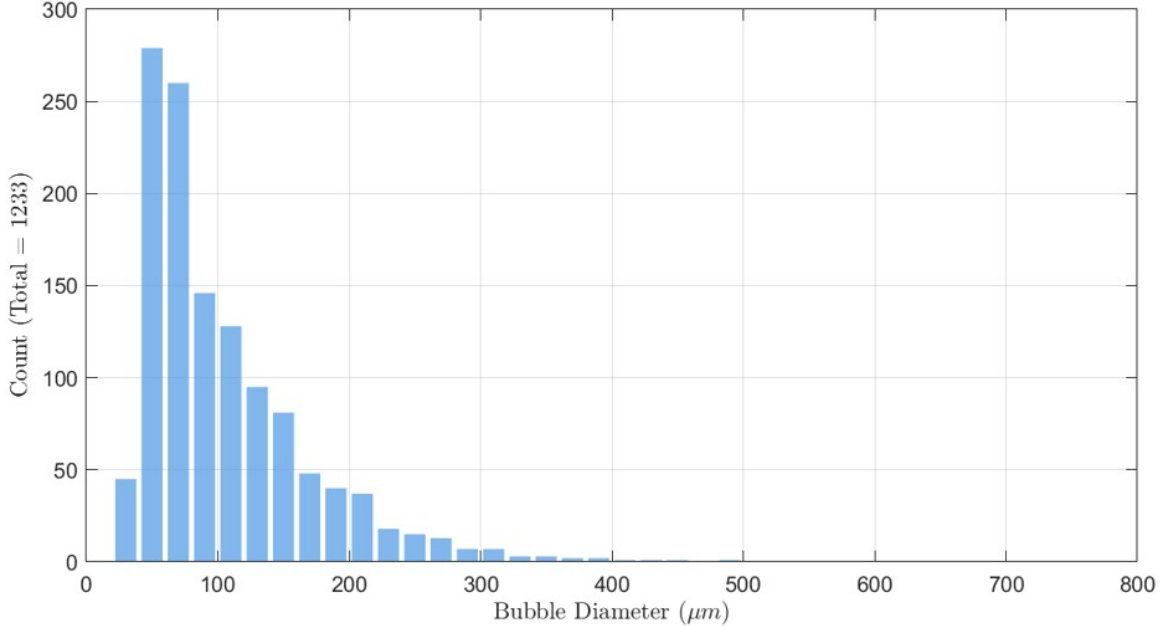


Figure 3.3: Bubble size distribution for 7° half-angle, 225°F, $\alpha = 0.2\%$.

with 0.2% air volume.

The established approach to cross compare results of Venturi microbubble generators for variations in operating parameters is to extract statistical data describing bubble size and distribution such as Sauter mean diameter, volume-equivalent mean diameter, and probability density functions (Gabbard, 1972; Li et al., 2017; Sun et al., 2017; Yin et al., 2015; Ruan et al., 2023). Probability density functions for this data are formed by modeling the bubble distributions as a log-normal distribution. If D is the set of all diameters, then $\ln D$ is approximated by a normal distribution $\ln D \sim \mathcal{N}(\mu_{LN}, \sigma_{LN}^2)$. The mean (μ_{LN}) and standard deviation (σ_{LN}) in the log-transformed space are calculated as follows:

$$\mu_{LN} = \frac{1}{N} \sum_{i=1}^N \ln D_i \quad (3.1)$$

$$\sigma_{LN} = \sqrt{\frac{1}{N} \sum_{i=1}^N (\ln D_i - \mu_{LN})^2} \quad (3.2)$$

The mean and standard deviation can then be used to generate the log-normal probability distribution (PDF) as follows.

$$f_D(d) = \frac{1}{d \sigma_{LN} \sqrt{2\pi}} \exp\left(-\frac{(\ln d - \mu_{LN})^2}{2\sigma_{LN}^2}\right) \quad (3.3)$$

A sample PDF is shown in Figure 3.4 for the same data as Figure 3.3 in both log-transformed (3.4a) and

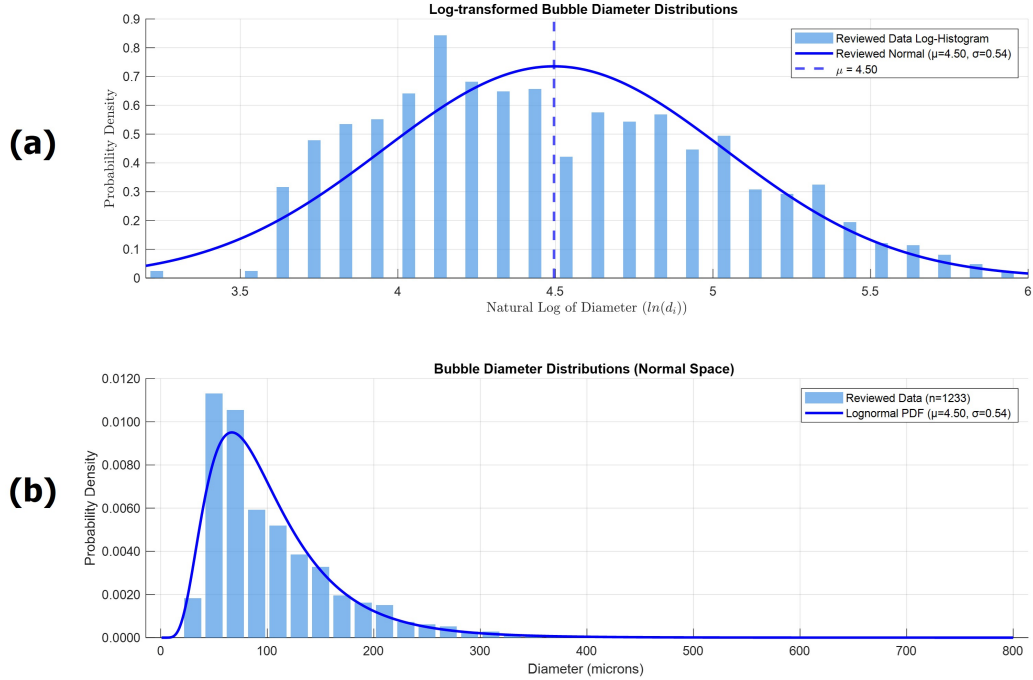


Figure 3.4: Probability density function for 7° half-angle, 225°F, $\alpha = 0.2\%$ in log (a) and normal (b) scales.

linear (3.4b) spaces.

Sauter mean diameter (d_{32}) and the volume-equivalent mean diameter (d_{30}) are defined in Equation 3.4 and Equation 3.5 respectively. The Sauter mean diameter yields the diameter of the sphere that has the same volume-to-surface area ratio as the particle population, and the volume-equivalent mean is the diameter of the sphere that yields the average particle volume. Sauter mean diameter is influenced by the presence of large outlier bubbles more than the volume-equivalent mean diameter, as spheres have the smallest surface-area to volume ratio. In the current study, emphasis is placed on the volume-equivalent mean diameter, d_{30} . Figure 3.5 shows the same data as Figure 3.4 in both log-transformed and linear spaces with the calculated PDF curves, with Sauter mean diameter and volume-equivalent mean diameter annotated.

$$d_{32} = \frac{\sum n_i d_i^3}{\sum n_i d_i^2} \quad (3.4)$$

$$d_{30} = \left(\frac{\sum n_i d_i^3}{\sum n_i} \right)^{1/3} \quad (3.5)$$

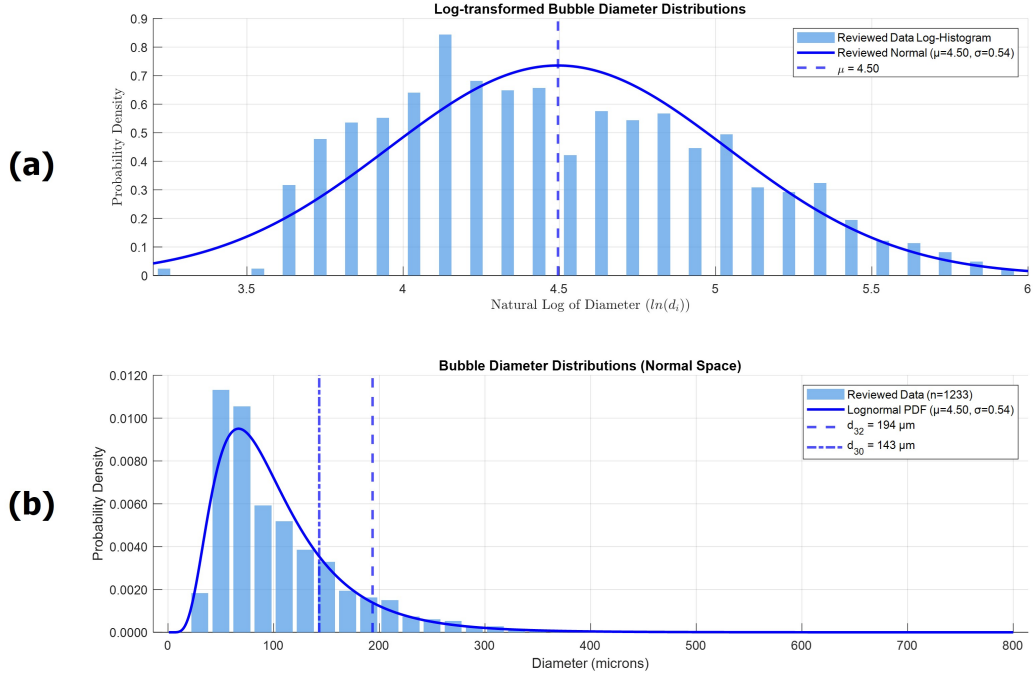


Figure 3.5: Probability density function for 7° half-angle, 225°F, $\alpha = 0.2\%$ in log (a) and normal (b) scales with d_{30} and d_{32} labeled.

To assess measurement consistency, all aeration trials for the typical 0.2% aeration were conducted twice. As illustrated in Figure 3.6, high repeatability was observed across key parameters including d_{32} , d_{30} , μ_{LN} , and σ_{LN} with R^2 values ranging from 0.92 to 0.97. The high R^2 values confirm the measurement methodology used for Venturi microbubble generation is robust and reproducible across independent runs. Due to the higher repeatability of d_{30} across all experiments, it was selected as the primary representative bubble diameter. Presented values in later analysis are the average of trial 1 and trial 2.

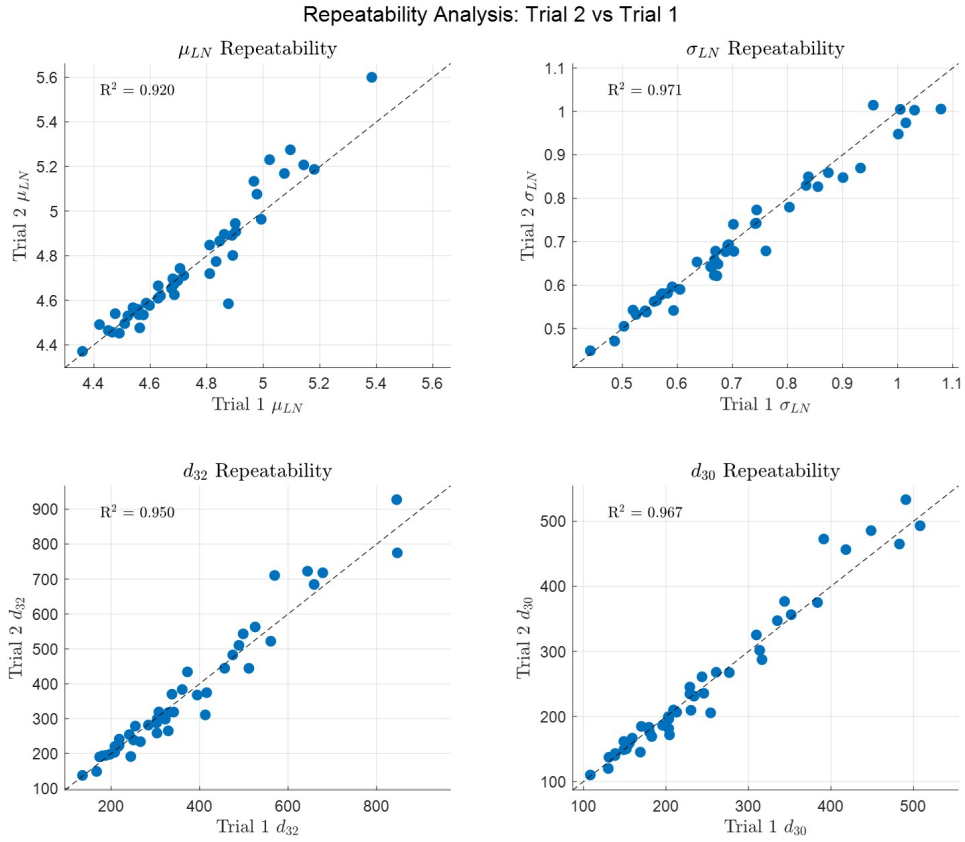


Figure 3.6: R^2 value between trial 1 and trial 2 statistical values derived from image processing for all temperatures, diverging half-angles, and flow rates at 0.2% aeration.

3.3 Effect of Flow Rate

The role of changing flow rate and its influence on bubble size distribution was first assessed by comparing probability density functions. Figure 3.7 shows typical bubble size probability density functions for the 15° Venturi nozzle with the working fluid operating at 225°F and 0.2% aeration for different flow rates. As flow rate increases, the PDFs shift leftward and become narrower, indicating smaller diameters and a more uniform size distribution. The volume-equivalent diameter, d_{30} , decreases with flow rate as indicated by the dashed lines.

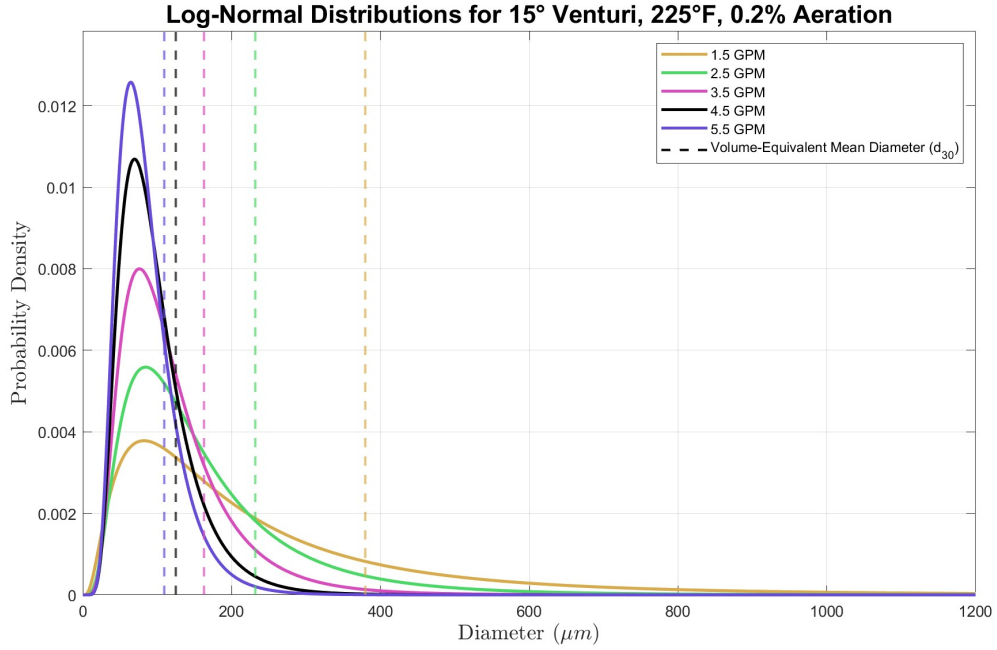


Figure 3.7: Probability density functions for all flow rates at $\beta = 15^\circ$, $225^\circ F$, $\alpha = 0.2\%$.

Figure 3.8 shows d_{30} and σ_{LN} as functions of flow rate for all three operating temperatures for the 15° nozzle. Increased flow rate consistently reduces d_{30} and σ_{LN} for all operating temperatures, indicating a more uniform and smaller distribution of bubble sizes driven by higher flow rate. Plots for other angles are presented in Appendix B.1.

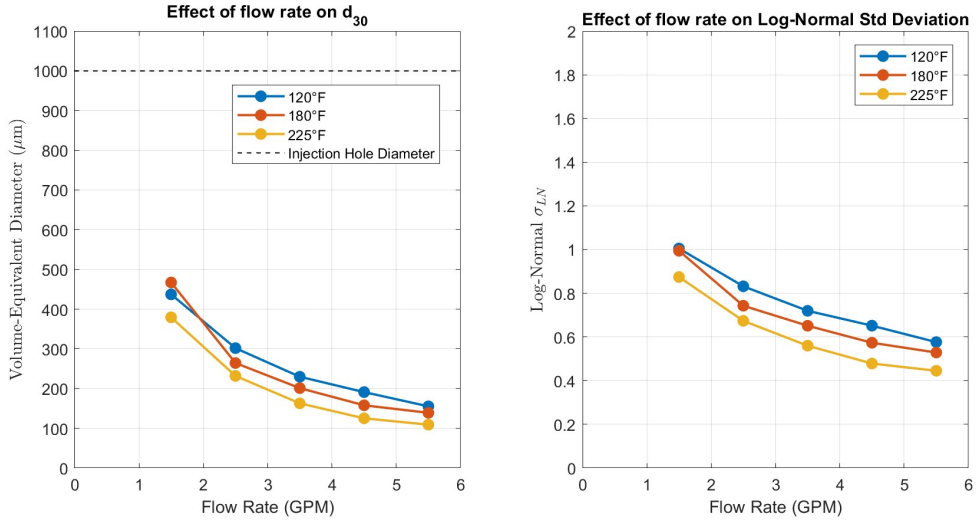


Figure 3.8: Effect of flow rate on bubble diameter, $\beta = 15^\circ$, $\alpha = 0.2\%$.

3.4 Effect of Diverging Angle

Figure 3.9 shows PDFs for the 5.5 GPM, 225°F trial for 7°, 15°, and 30° Venturi half-angles. For this operating condition, the 15° half-angle shows better performance. The clarity of this differentiation between different Venturi nozzles is more discernible in the high flow rate regime as compared to lower flow rates.

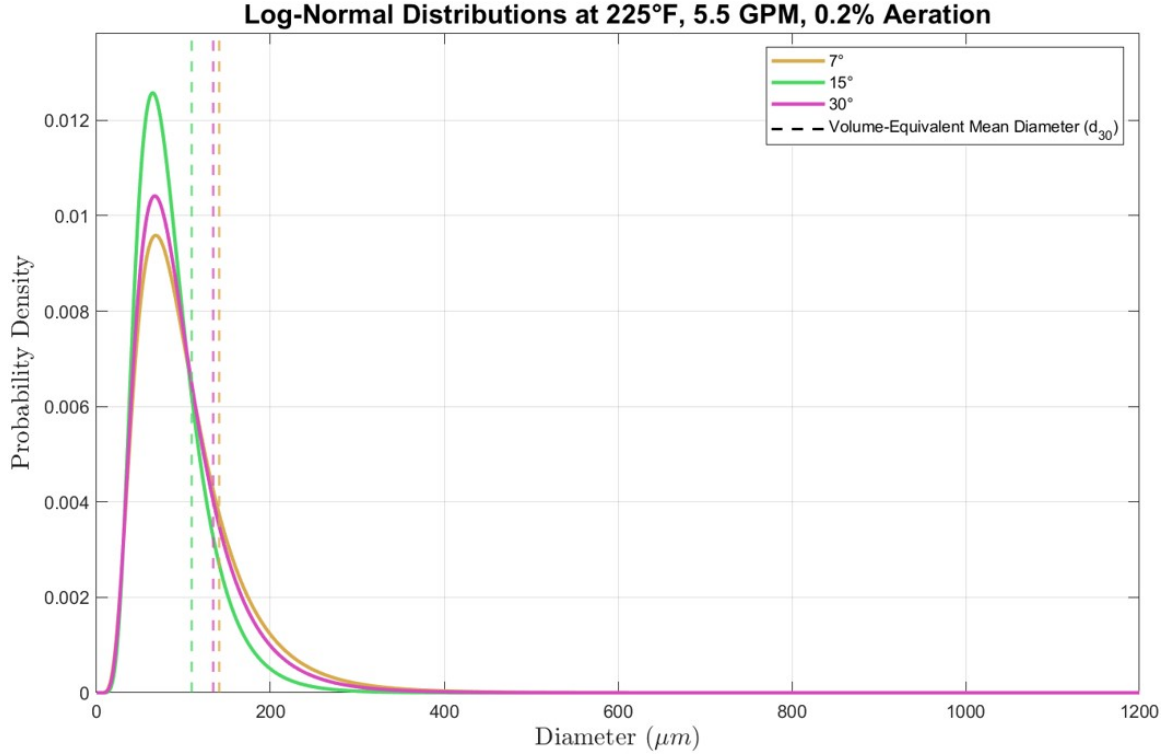


Figure 3.9: PDF distributions for all angles 5.5 GPM, 225°F, $\alpha = 0.2\%$.

Volume-equivalent diameter and log-normal standard deviation for the three different Venturi half-angles in this study are shown in Figure 3.10 for all temperatures at 5.5 GPM. Better performance of the 15° nozzle is evident by the smaller equivalent diameter and decreased spread of bubble diameters. Accompanying data is found in Appendix B.2 for other flow rates.

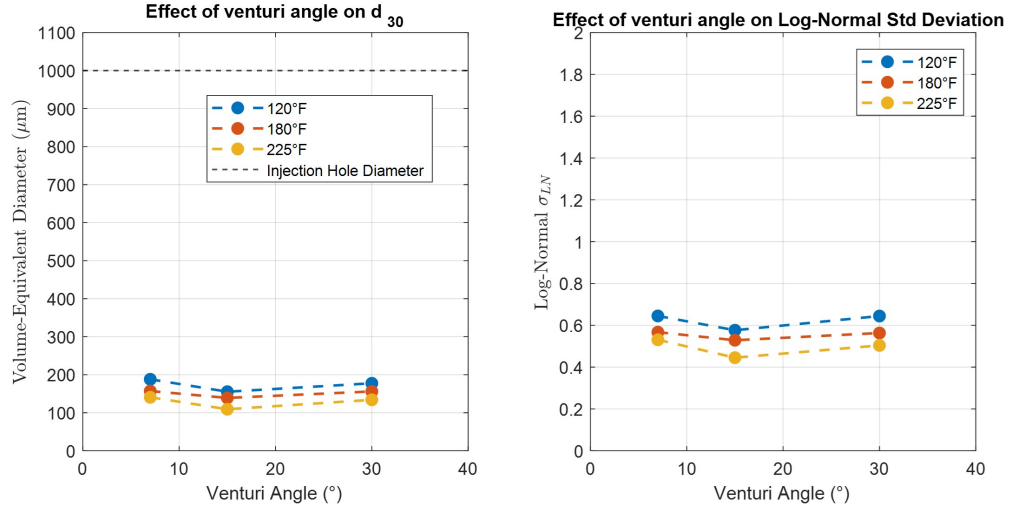


Figure 3.10: Effect of Venturi angle β on bubble characteristics at 5.5 GPM, $\alpha = 0.2\%$.

3.5 Effect of Temperature (Viscosity and Surface Tension)

Viscosity and surface tension were varied through temperature control to assess their influence on bubble fragmentation. Figure 3.11 shows the variation of viscosity and surface tension across the experimental temperature range as discussed in Section 1.3.

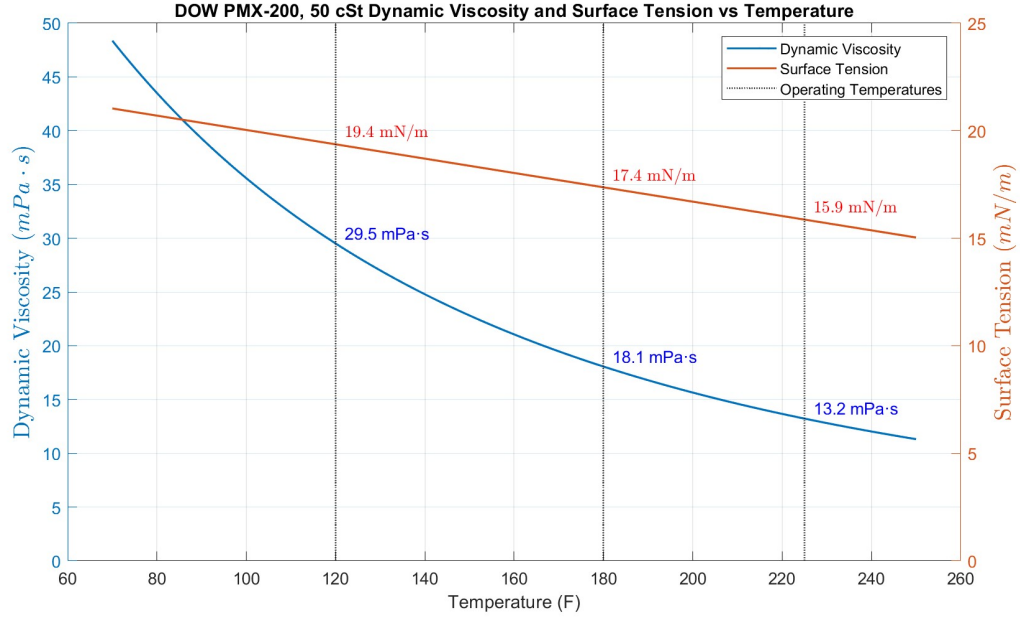


Figure 3.11: DOW PMX-200 Series Variation of Surface Tension and Viscosity with Temperature.

The variation of d_{30} and σ_{LN} with temperature is shown in Figure 3.12 for the 15° Venturi nozzle, with other angles presented in Appendix B.3. As viscosity and surface tension decrease with increasing temper-

ture, both d_{30} and σ_{LN} decrease, indicating the role of decreased viscosity and surface tension driving bubble fragmentation.

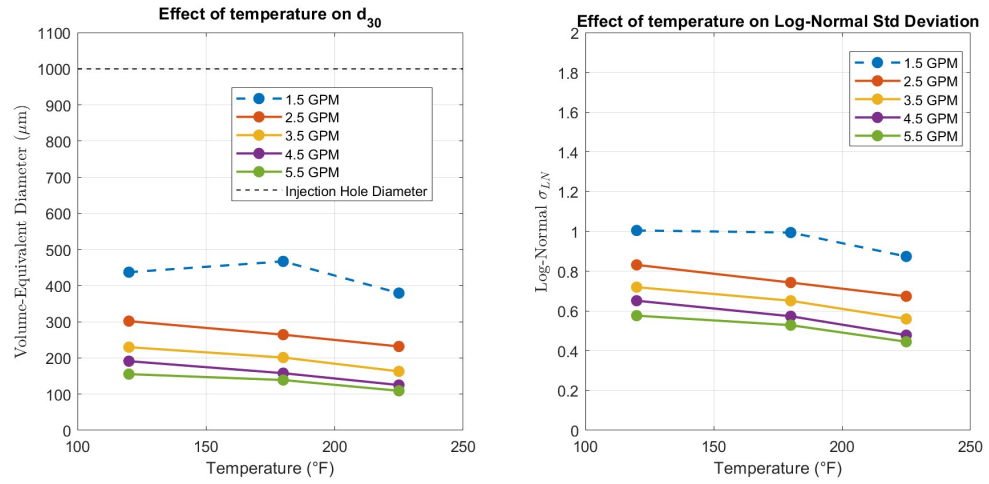


Figure 3.12: Effect of temperature on bubble characteristics, $\beta = 15^\circ$, $\alpha = 0.2\%$.

CHAPTER 4

Empirical Analysis

Experimental data of the present study has been compared with results from prior studies in water-air systems Yin et al. (2015); Sun et al. (2017) across the three nondimensional parameters: Reynolds, Capillary, and Weber numbers. Volume-equivalent diameter (d_{30}) data from the present study's extensive 15° half-angle Venturi experiments has been used to compare with the reference studies.

Yin et al. (2015) used a 23 mm diameter Venturi throat with a diverging half-angle of 8°; data was extracted from their Figure 7 for the 0.2% aeration case utilizing WebPlotDigitizer (Rohatgi, 2025). This data was re-normalized to use throat diameter instead of inlet diameter as the characteristic length scale. Sun et al employed a 25 mm Venturi throat and 7.5° diverging half-angle; data was extracted from their Figure 13b with 0.2% – 0.4% aeration fraction. These reference studies were selected for their use of the same representative diameter d_{30} , as well as the presence of sufficient information about geometries and flow conditions to extract working nondimensional parameters.

4.1 Reynolds Number Investigation

Figure 4.1 shows normalized bubble diameter d_{30}/D_t vs Reynolds number $\left(\frac{\rho V_t D_t}{\mu}\right)$ for the current 15° nozzle at all three operating temperatures. The dashed black line indicates the normalized air injection hole diameter. There is a clear trend of decreasing bubble size with increasing Reynolds number. Power-law fits for normalized bubble diameter for each temperature show exponents for Re ranging from -0.76 to -0.98, consistent with prior Reynolds fragmentation models (Gabbard (1972); Sun et al. (2017); Yin et al. (2015); Zhao et al. (2019)). The plot primarily displays the trend of reduced bubble size with increased flow velocity. As Re increases, the data converges, suggesting that inertial forces dominate and viscosity plays a diminished role.

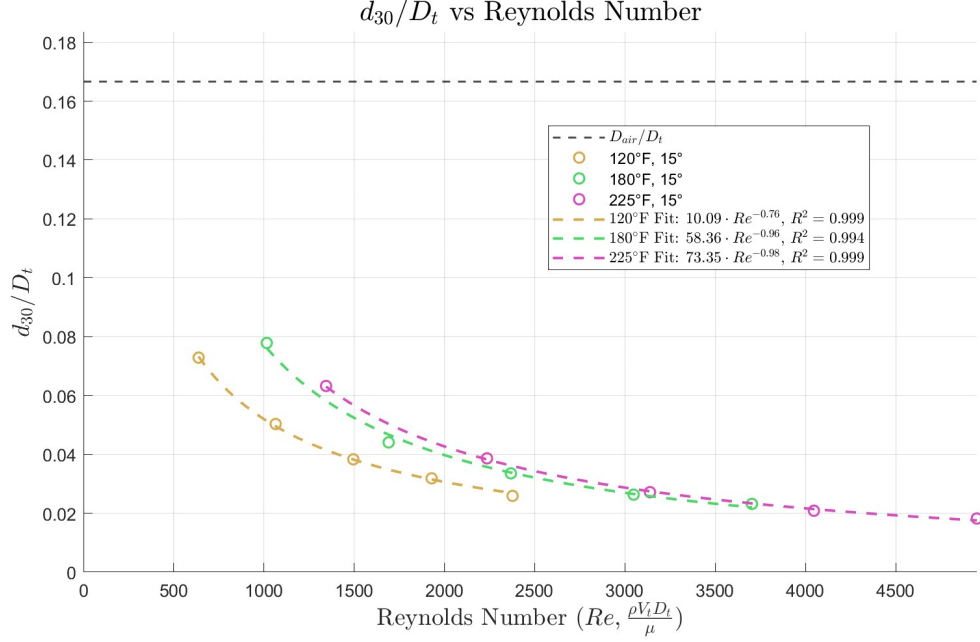


Figure 4.1: d_{30}/D_t vs Reynolds for present study at 15° Venturi angle.

In Figure 4.2, the 15° Venturi data of the present study is plotted alongside reference water aeration data from Yin et al. (2015) and Sun et al. (2017) in linear (4.2a) and log-scales (4.2b). The current data is novel in that it captures bubble fragmentation in the lower Reynolds number regime typical of a viscous working fluid. Figure 4.2 highlights the fact that that Reynolds number alone is not sufficient to find parity between current and existing data, since the former deals with a viscous oil-air system and the latter deals with a water-air system. This motivates further analysis with metrics that include surface tension and viscosity such as the Weber and Capillary numbers.

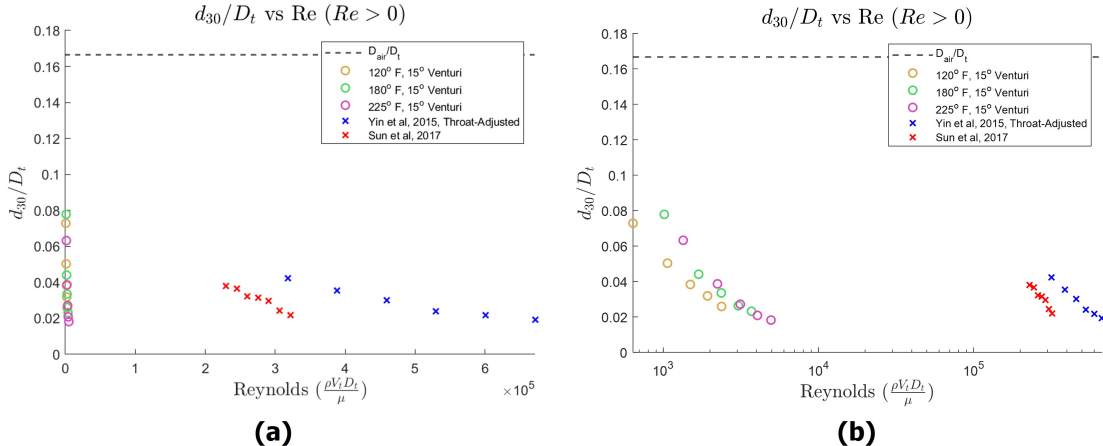


Figure 4.2: d_{30}/D_t vs Reynolds for present study and Yin et al. (2015); Sun et al. (2017).

4.2 Capillary Number Investigation

Figure 4.3 shows the relationship between normalized bubble diameter d_{30}/D_t and Capillary number $\left(\frac{\mu V_t}{\sigma}\right)$ for the 15° Venturi with constant flow rate lines for each tested flow rate. Capillary number represents the ratio of viscous shear to surface tension. Bubble size decreases with increasing Capillary number for all operating temperatures, demonstrating the coupling between fluid velocity and viscous shear.

The constant-flow-rate trend lines provide further insight. For a fixed flow rate, moving leftwards along an iso-flow results in smaller bubbles. In this scenario, both μ and σ are decreasing due to the temperature rise, but μ is decreasing by a larger percentage, so capillary number decreases. The slope of these iso-flow lines becomes shallower at higher flow rates, implying that the bubble size depends less on fluid properties, and increasingly on the flow inertia, diminishing the predictive power of the Capillary number.

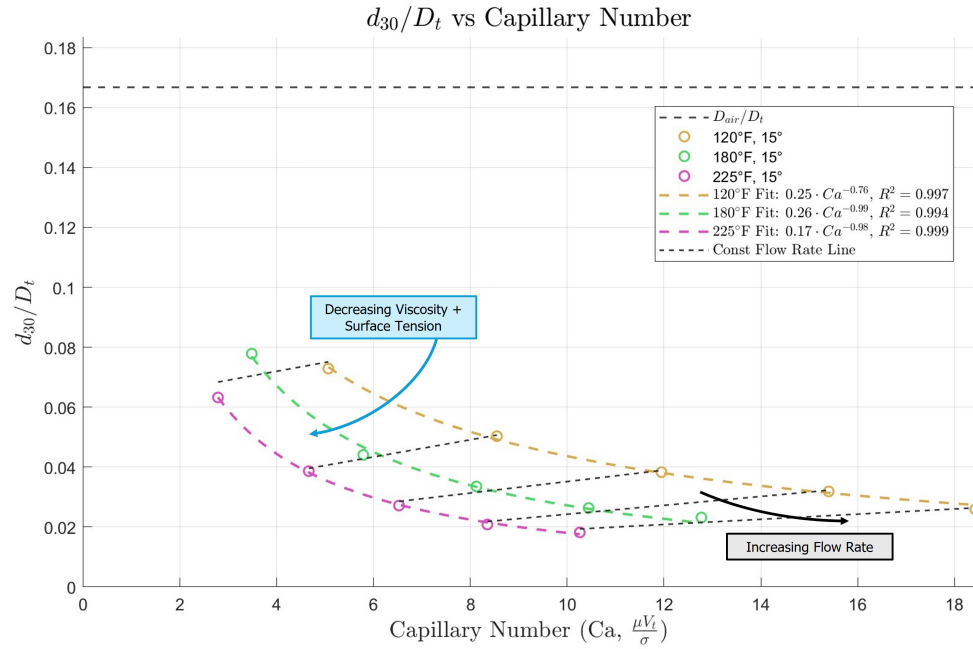


Figure 4.3: d_{30}/D_t vs Capillary for present study at 15° Venturi angle.

Normalized bubble diameter $\frac{d_{30}}{D_t}$ and Capillary number data from the present study data is compared with water aeration data from Yin et al. (2015) and Sun et al. (2017) in both regular (Figure 4.4b) and log-scale (Figure 4.4b) plots. Neither the Reynolds nor the Capillary number alone provides sufficient avenue for developing a universal understanding.

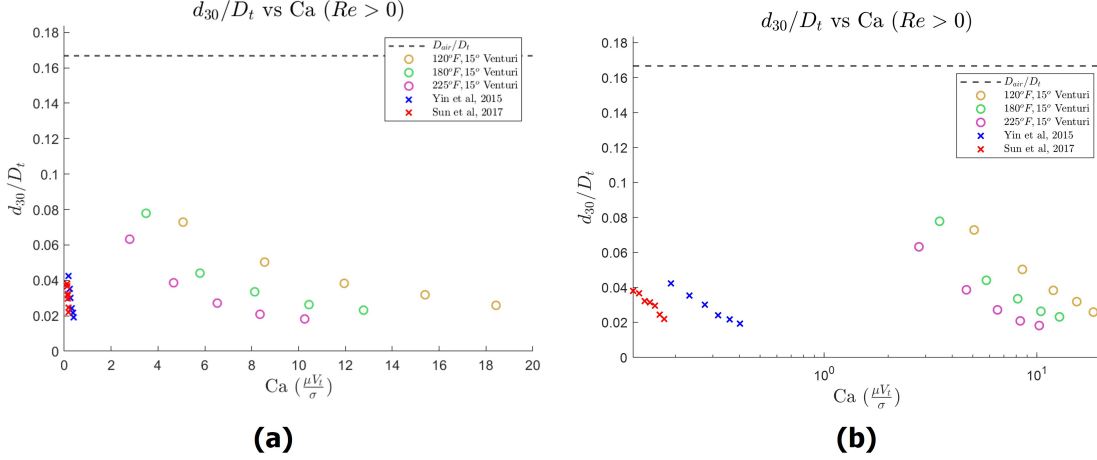


Figure 4.4: d_{30}/D_t vs Capillary for present study and Yin et al. (2015); Sun et al. (2017).

4.3 Weber Number Investigation

Figure 4.5 shows the normalized bubble diameter data from the present study as a function of Weber $\left(\frac{\rho V_t^2 D_t}{\sigma}\right)$ number for the 15° Venturi for all operating temperatures. Weber number directly accounts for the contribution of flow energy towards bubble fragmentation. There is a closer clustering of the three temperature curves, showing a stronger dependence on flow energy, and a weaker dependence on fluid viscosity.

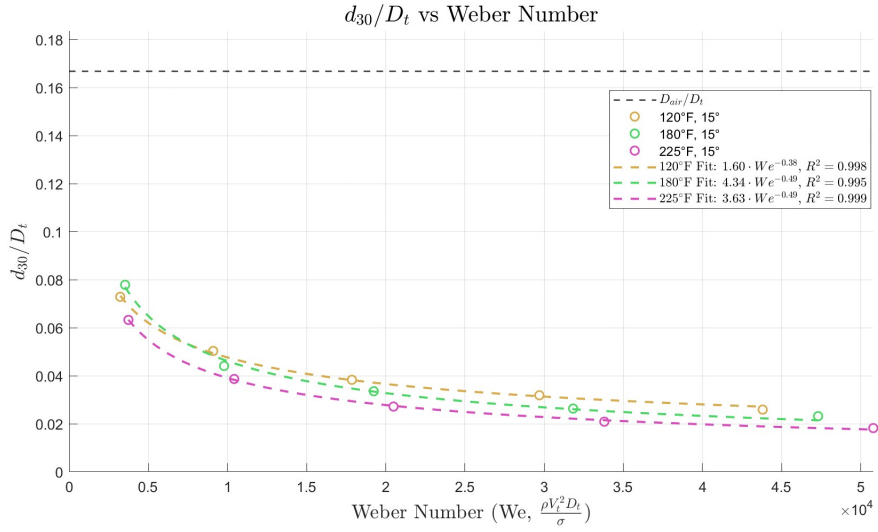


Figure 4.5: d_{30}/D_t vs Weber for present study at 15° Venturi angle.

In Figure 4.6, bubble diameter vs Weber number data from the present oil aeration study is plotted alongside water aeration data from Yin et al. (2015) and Sun et al. (2017) in both linear (4.6a) and log (4.6b) scales. Though a universal trend cannot be established, the Weber number groups the various viscosity data better than Reynolds or Capillary numbers, suggesting a diminished role for viscosity.

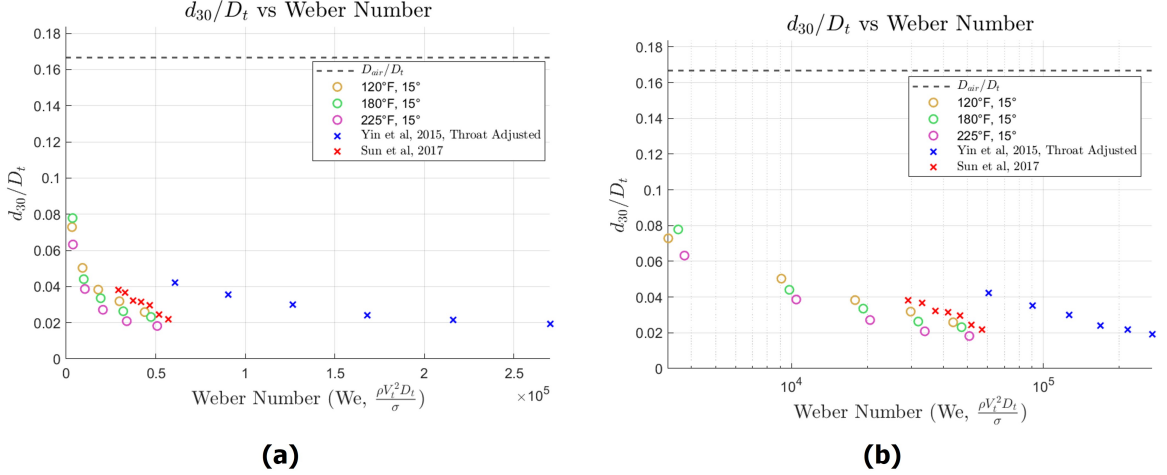


Figure 4.6: d_{30}/D_t vs Weber for present study and Yin et al. (2015); Sun et al. (2017).

4.4 Universality Investigation

Building upon the earlier dimensionless analysis (Equation 1.3) and using the current extensive data on controlled variation of fluid viscosity and surface tension, a universal fit of the form $\frac{d_{30}}{D_t} = Re^a \cdot We^b$ has been examined in Figure 4.7a, including reference water-air data. While the plot looks to have some universality, the correlation's low R^2 value of 0.855 indicates that it fails to capture the detailed variations of fluid viscosity and surface tension of the current study. Restricting analysis to the regime of the current investigation, a Weber-Reynolds fit with a high correlation coefficient ($R^2 = 0.970$) has been fitted in Figure 4.7b. A similar inconsistency is observed when the analysis is conducted for the Reynolds-Capillary relationship (Figure 4.8). The current investigation proved the need to address surface tension and viscosity through Weber and Capillary numbers in developing an analytical model for Venturi-based fragmentation.

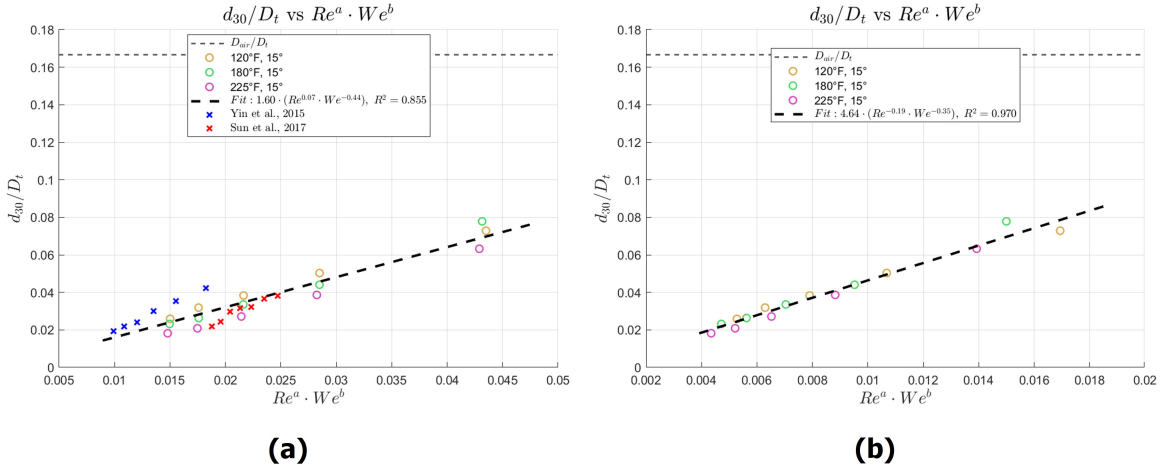


Figure 4.7: d_{30}/D_t vs $Re^a \cdot We^b$ fit including (a) and excluding external data from (b) Yin et al. (2015); Sun et al. (2017).

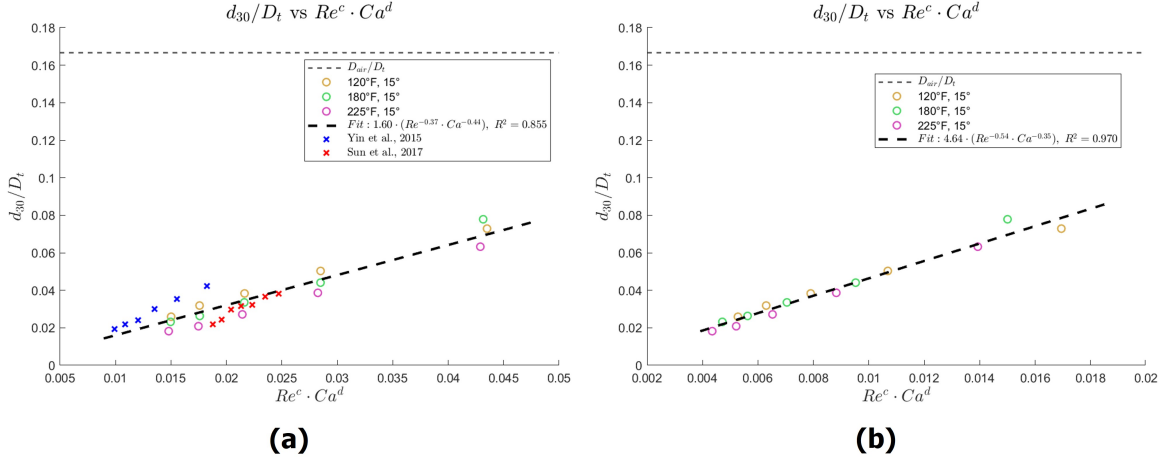


Figure 4.8: d_{30}/D_t vs $Re^c \cdot Ca^d$ fit including (a) and excluding external data from (b) Yin et al. (2015); Sun et al. (2017).

CHAPTER 5

Discussion

In the present novel study, transient Venturi-based aeration has been examined in a homogeneous, viscous medium with flow rate and temperature control. This novel investigation is distinct from previous investigations which have been predominantly limited to water-air systems. Our studies in viscous fluids have pointed out that any viscous fluid can fragment bubbles provided there is sufficient flow energy. The Reynolds number establishes the entry flow criteria, whereas the Weber number better captures the bubble fragmentation regardless of the fluid viscosity.

The dimensionless volume-equivalent bubble diameter data has been examined as a function of Reynolds number, Capillary number, and Weber number. Bubble fragmentation is better captured through the Weber number, indicating that flow energy is the main arbiter in bubble fragmentation. A suitable combination of any two numbers (Re,Ca or Re,We) is able to collapse the current data into a universal fit with a high degree of correlation, highlighting the role of fluid transport energy, viscous shear, and surface tensile forces in bubble breakup. However, a universal fit between the present experimental data with existing data for high Reynolds number water-air systems has not been established. This implies the need for an improved analytical framework which includes the role of fluid viscosity and bubble surface tension in modeling bubble fragmentation. Such advances would also aid development of machine learning predictive models for bubble generation.

Future work will aim to broaden the operational regime by incorporating lower-viscosity fluids. From an application standpoint, Venturi-based aeration in viscous media could be enhanced by exploring the effects of flow recirculation, where repeated passes through the injector may promote further bubble fragmentation. Additionally, geometric modifications to the diverging section of the Venturi nozzle such as surface roughness may improve bubble breakup efficiency and should be investigated in future studies.

References

- Agarwal, A., Ng, W. J., and Liu, Y. (2011). Principle and applications of microbubble and nanobubble technology for water treatment. *Chemosphere*, 84(9):1175–1180.
- Bhat, A. A., Chen, Y.-W., Liang, Y.-S., Chen, S.-Y., Hsieh, C.-W., Lin, C.-M., Chen, M.-H., Huang, P.-H., Shih, M.-K., and Hou, C.-Y. (2025). Exploring the Potential of Microbubble Innovation in Revolutionizing Food Industry: A Comprehensive Review. *Food and Bioprocess Technology*, 18(5):4175–4194.
- Budhijanto, W., Darlianto, D., Pradana, Y. S., and Hartono, M. (2017). Application of micro bubble generator as low cost and high efficient aerator for sustainable fresh water fish farming. page 110008, East Java, Indonesia.
- Darhuber, A. A., Davis, J. M., Troian, S. M., and Reisner, W. W. (2003). Thermocapillary actuation of liquid flow on chemically patterned surfaces. *Physics of Fluids*, 15(5):1295–1304.
- DowChemicalCompany (2017). XIAMETER PMX-200 Silicone Fluid, 5-20 cSt. Technical report, The Dow Chemical Company.
- DowChemicalCompany (2024). XIAMETER PMX-200 Silicone Fluid, 50-1000 cSt. Technical report, The Dow Chemical Company.
- Gabbard, C. H. (1972). Development of a Venturi Type Bubble Generator for Use in the Molten-Salt Reactor Xenon Removal System. Technical Report ORNL-TM-4122, 12784156, Oak Ridge National Laboratory.
- Gordiychuk, A., Svanera, M., Benini, S., and Poesio, P. (2016). Size distribution and Sauter mean diameter of micro bubbles for a Venturi type bubble generator. *Experimental Thermal and Fluid Science*, 70:51–60.
- Hinze, J. O. (1955). Fundamentals of the hydrodynamic mechanism of splitting in dispersion processes. *AIChE Journal*, 1(3):289–295.
- Li, J., Song, Y., Yin, J., and Wang, D. (2017). Investigation on the effect of geometrical parameters on the performance of a venturi type bubble generator. *Nuclear Engineering and Design*, 325:90–96.
- Lu, J., Jones, O. G., Yan, W., and Corvalan, C. M. (2023). Microbubbles in Food Technology. *Annual Review of Food Science and Technology*, 14(1):495–515.
- Mathworks (2025). Image processing toolbox: (r2023b).
- Murai, Y., Tasaka, Y., Oishi, Y., and Ern, P. (2021). Bubble fragmentation dynamics in a subsonic Venturi tube for the design of a compact microbubble generator. *International Journal of Multiphase Flow*, 139:103645.
- Nomura, Y., Uesawa, S.-i., Kaneko, A., and Abe, Y. (2011). Study on Bubble Breakup Mechanism in a Venturi Tube. In *ASME-JSME-KSME 2011 Joint Fluids Engineering Conference: Volume 1, Symposia – Parts A, B, C, and D*, pages 2533–2540, Hamamatsu, Japan. ASMEDC.
- Roberts, C., Graham, A., Nemer, M., Phinney, L., Garcia, R., Soehnel, M., and Stirrup, E. (2017). Physical Properties of Low-Molecular Weight Polydimethylsiloxane Fluids. Technical Report SAND2017-1242, 1343365, 651009, Sandia National Laboratories.
- Robertson, R., Smith, O., Briggs, R., and Bettis, E. (1970). ORNL-4528.pdf.
- Rohatgi, A. (2025). Webplotdigitizer. Available at <https://automeris.io/WebPlotDigitizer>.
- Ruan, J., Zhou, H., Ding, Z., Zhang, Y., Zhao, L., Zhang, J., and Tang, Z. (2023). Machine learning-aided characterization of microbubbles for venturi bubble generator. *Chemical Engineering Journal*, 465:142763.

- Schepner, C., Smith, A., Schafer, D., and Anilkumar, A. (2023). In Situ Assessment of Oil Quality Sensor Performance in Engine Lubricant Flow. *SAE International Journal of Fuels and Lubricants*, 17(2):04–17–02–0007.
- Sharma, P. K., Gibcus, M. J., Van Der Mei, H. C., and Busscher, H. J. (2005). Influence of Fluid Shear and Microbubbles on Bacterial Detachment from a Surface. *Applied and Environmental Microbiology*, 71(7):3668–3673.
- Smith, A. D. and Anilkumar, A. V. (2022). Friction Factor Evaluation of Replaceable-Element and Conventional Oil Filters in a Precision Benchtop Test Facility. *SAE International Journal of Fuels and Lubricants*, 15(3):255–264.
- Sun, L., Mo, Z., Zhao, L., Liu, H., Guo, X., Ju, X., and Bao, J. (2017). Characteristics and mechanism of bubble breakup in a bubble generator developed for a small TMSR. *Annals of Nuclear Energy*, 109:69–81.
- Terasaka, K., Hirabayashi, A., Nishino, T., Fujioka, S., and Kobayashi, D. (2011). Development of microbubble aerator for waste water treatment using aerobic activated sludge. *Chemical Engineering Science*, 66(14):3172–3179.
- Yin, J., Li, J., Li, H., Liu, W., and Wang, D. (2015). Experimental study on the bubble generation characteristics for an venturi type bubble generator. *International Journal of Heat and Mass Transfer*, 91:218–224.
- Zhao, L., Huang, J., Chen, C., and Gao, J. (2024). Investigations on the near-wall bubble dynamic behaviors in a diverging channel. *AIP Advances*, 14(11):115014.
- Zhao, L., Sun, L., Mo, Z., Du, M., Huang, J., Bao, J., Tang, J., and Xie, G. (2019). Effects of the divergent angle on bubble transportation in a rectangular Venturi channel and its performance in producing fine bubbles. *International Journal of Multiphase Flow*, 114:192–206.

APPENDIX

Appendix A

Facility Information

A.1 LabVIEW Interface

The Venturi microbubble aeration experiment was operated using a custom LabVIEW program that integrated real-time measurement, control, and data logging. The user interface (Figure A.1) enables control of the solenoid valve, monitoring and control of air flow rates, and recording of pressure and temperature signals. The solenoid can be triggered either through a timed pulse with adjustable duration or direct manual activation. Air flow rate is set as a fraction of the oil flow rate (in GPM) and converted to a milliliter-per-minute value, which is used to generate an analog control voltage for the mass flow controller. The measured air flow is displayed alongside the setpoint.

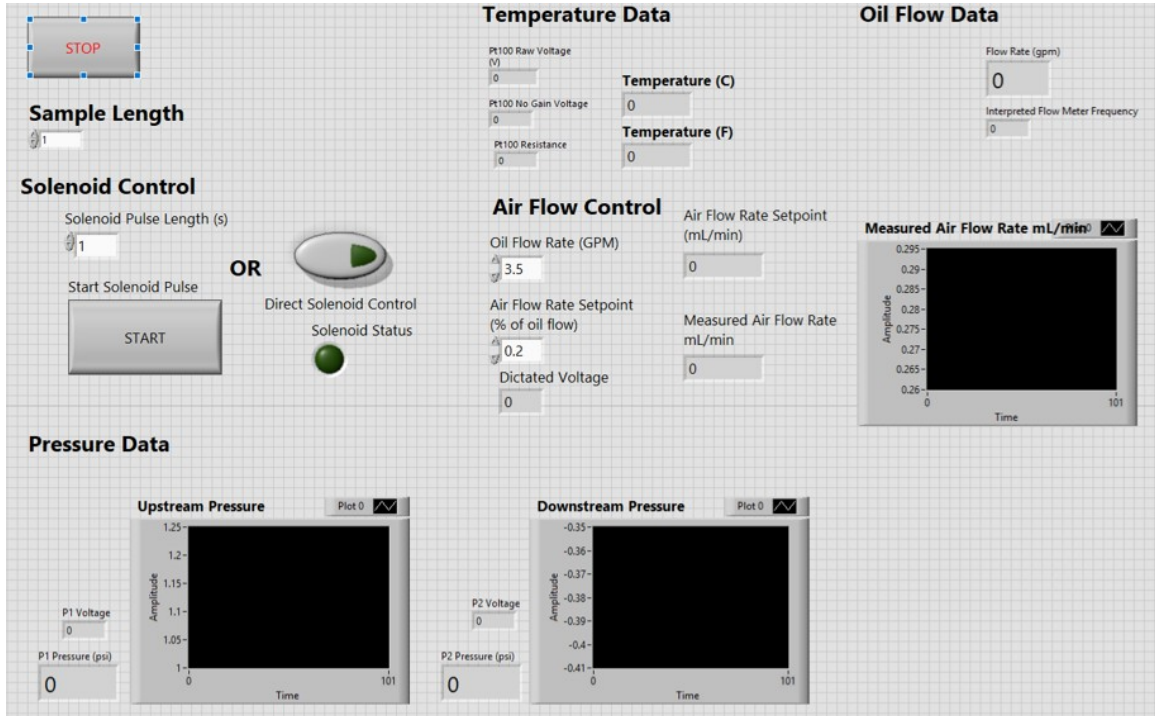


Figure A.1: LabVIEW Graphical User Interface for measurement, data logging, and facility control.

The underlying LabVIEW block diagram (Figure A.2) shows the signal flow and data processing logic. It includes acquisition from the DAQ module, control voltage generation for air injection, implementation of the temperature model, and display of measured data. The control loop architecture ensures that all data is tightly synchronized with an adjustable sample rate.

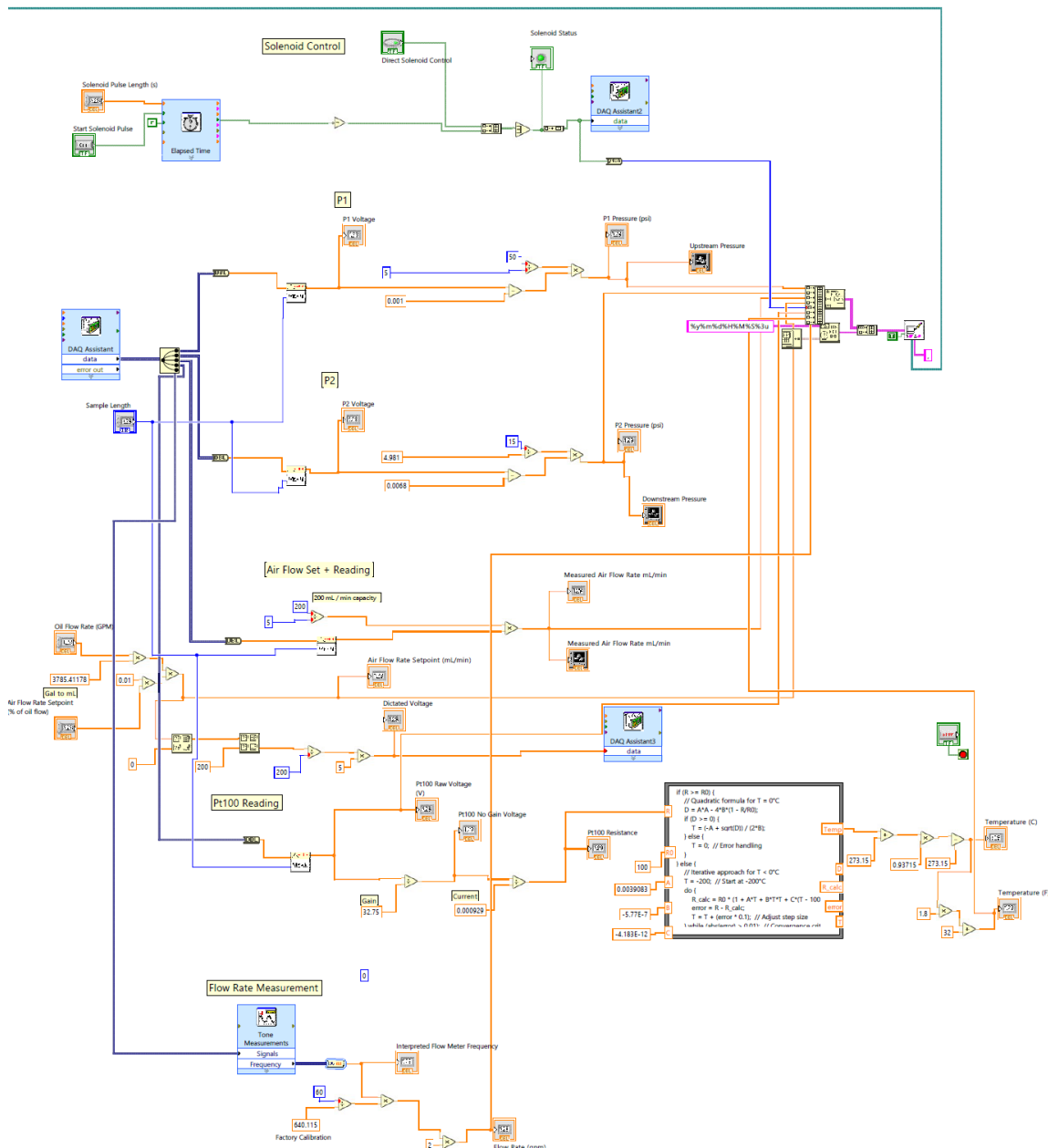


Figure A.2: LabVIEW back panel for measurement, data logging, and facility control.

A.2 Data Acquisition and Control Circuit

A custom data acquisition and control circuit was designed (Figure A.3) and assembled in-house to integrate all sensors and actuators used in the Venturi aeration experimental setup. This setup provided low-noise signal acquisition and reliable control for all experimental operations.

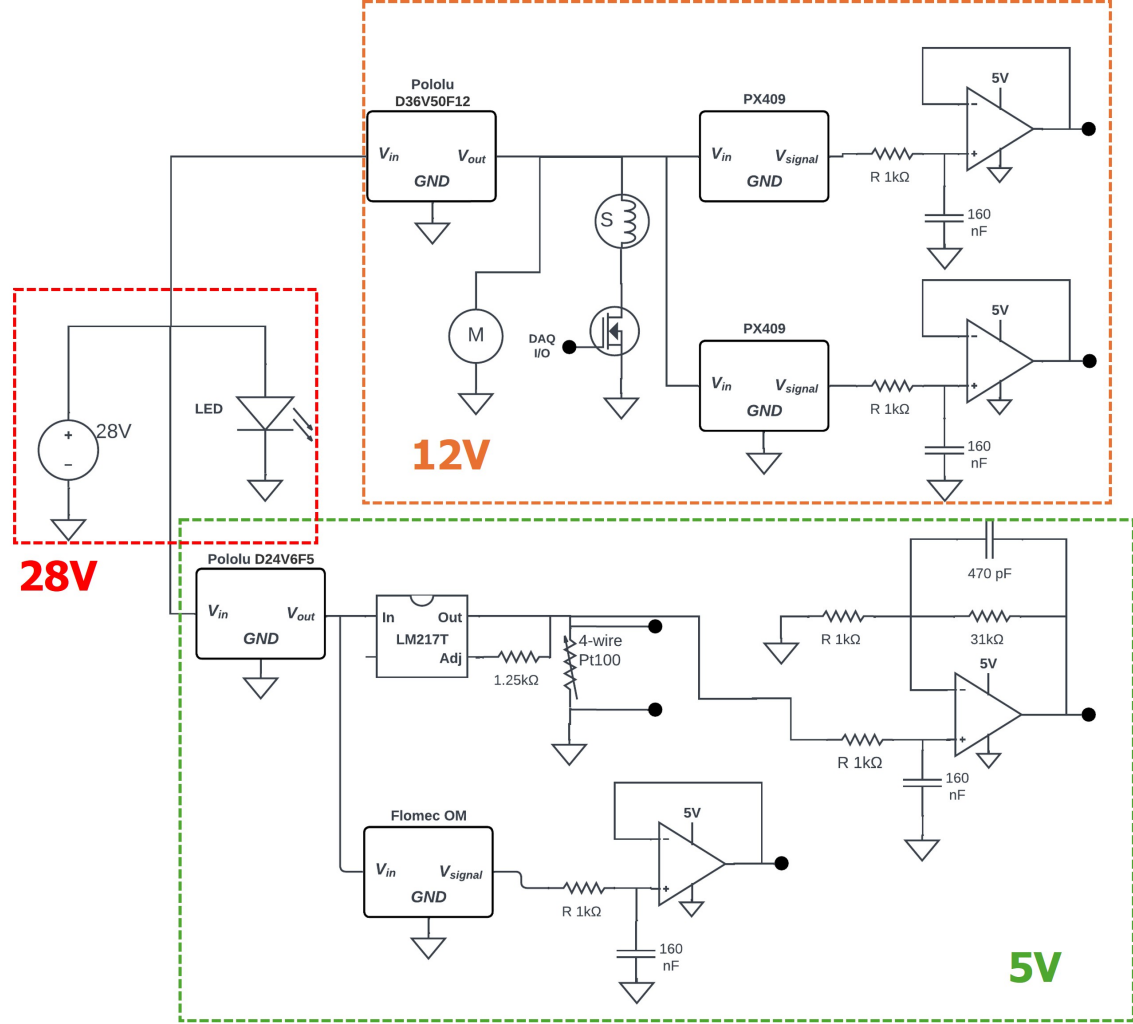


Figure A.3: Designed data acquisition and control circuitry.

A single commercial 28VDC power supply is routed to two commercial Pololu step-down regulators (12V and 5V) for various components. The LED system operates at 28V and 3A and is paired with a 12V DC fan to prevent overheating. The solenoid valve is actuated by a low-side NMOS switch controlled by the user from the LabVIEW interface. Two PX409 pressure transducers have shielded wires and provide 0–5V analog outputs, each passed through a 1 kHz active low-pass filter to suppress high-frequency noise. The Pt100 temperature sensor operates as a four-wire Class A configuration, powered by a constant 1 mA current source. Its signal is amplified using a non-inverting operational amplifier with a gain of 33 V/V and also filtered with a 1 kHz low-pass circuit. Calibration of the temperature sensor can be found in Section A.2.

The oil flowmeter hall-effect RPM sensor receives and outputs a 5V, and its output is processed through an active 1 kHz low-pass filter to reduce noise. A 5.5 GPM flow rate corresponds to pulse frequencies up to 60 Hz, so pulse signal is not attenuated by the 1 kHz filter. The air mass flow controller interface allows for reading and setting air flow parameters in the range of 0–200 mL/min using a 5V analog signal.

Assembled in-house, the circuit consists of two vertically stacked circuit boards that snap together, as shown in Figure A.4. The lower board (A.4a) houses the solenoid driver, filters and amplifiers, and constant current source for the RTD. The upper board snaps into the lower board (A.4b) and contains connectors for power and sensor connections. XT-90 connectors were used for high-current devices such as the LED and solenoid valve, while JST connectors routed power and signal lines for lower-power sensors including pressure transducers, the flow meter, Pt100 temperature sensor, and mass flow controller.

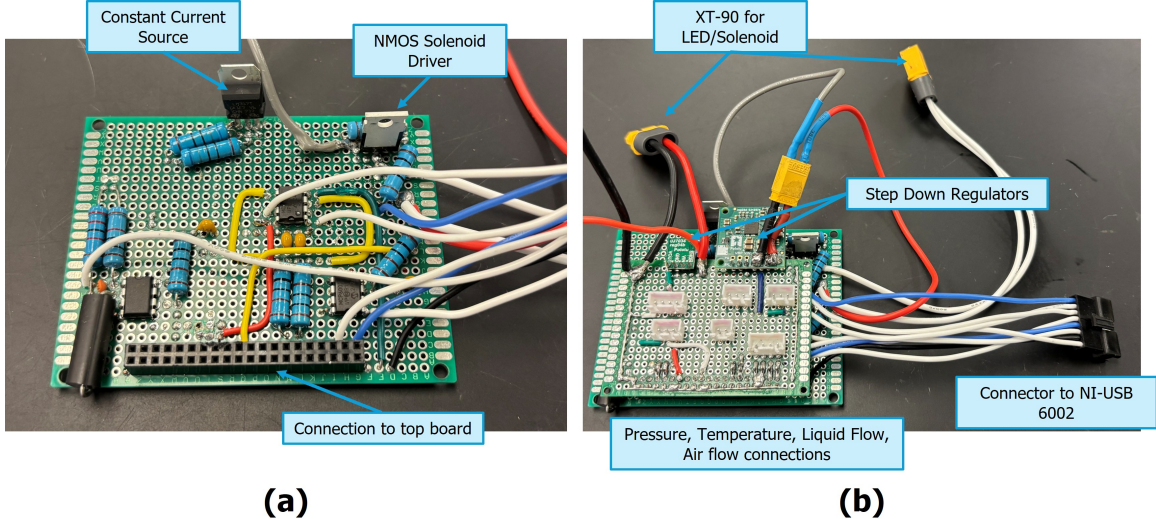


Figure A.4: Data acquisition and control circuit.

A.3 Temperature Calibration

To enable accurate temperature measurements from ambient conditions up to 250°F, a four-wire Class A Pt100 RTD was operated with a 1 mA constant current source which minimizes self-heating and is not negatively impacted by lead wire resistance. As described in Section A.2, the RTD was interfaced through an amplifier with a gain of approximately 33. This gain was selected to match the RTD's output range to the analog input range of the DAQ system and is based on the Pt100's characteristic resistance-temperature relationship governed by the Callendar–Van Dusen (CVD) equation A.1:

$$\text{For } T > 0^\circ\text{C} : R_{pt100} = R_0 \cdot (1 + AT + BT^2 + (CT^3 \cdot (T - 100))) \quad (\text{A.1})$$

Where R_0 is the Pt100 resistance at 0°C 100Ω , $A = 3.908310^{-3}$, $B = -5.77510^{-7}$, and $C = -4.18310^{-12}$. Ignoring higher-order terms, the simplified quadratic version of this equation:

$$R_{pt100} = R_0 \cdot (1 + AT + BT^2) \quad (\text{A.2})$$

is solved in LabVIEW immediately upon sampling. In the temperature range of interest, this simplification yields errors $< 0.05^\circ\text{C}$.

To calibrate the temperature sensing hardware, the Pt100 was benchmarked against two reference thermometers, one digital and one high-precision Hg thermometer, immersed in an ice bath and slowly heated to boiling over the course of 80 minutes while being stirred with a magnetic mixer. Measurements from all devices were simultaneously recorded every 2 minutes, and the experiment was repeated for two independent trials on February 12 and February 13, 2025. Pt100 temperature readings were then compared against the average of the mercury and digital thermometers. As shown in Figure A.5, the Pt100 response exhibited strong linear agreement with the references, with R^2 values of 0.9997 and 1.000 across the two trials. The average of the fitted slopes yielded the correction equation:

$$T(K) = 0.93715 \times T_{Pt100}(K) \quad (\text{A.3})$$

This adjustment was incorporated directly into the LabVIEW for all trials to ensure accurate temperature readings and determination of fluid properties.

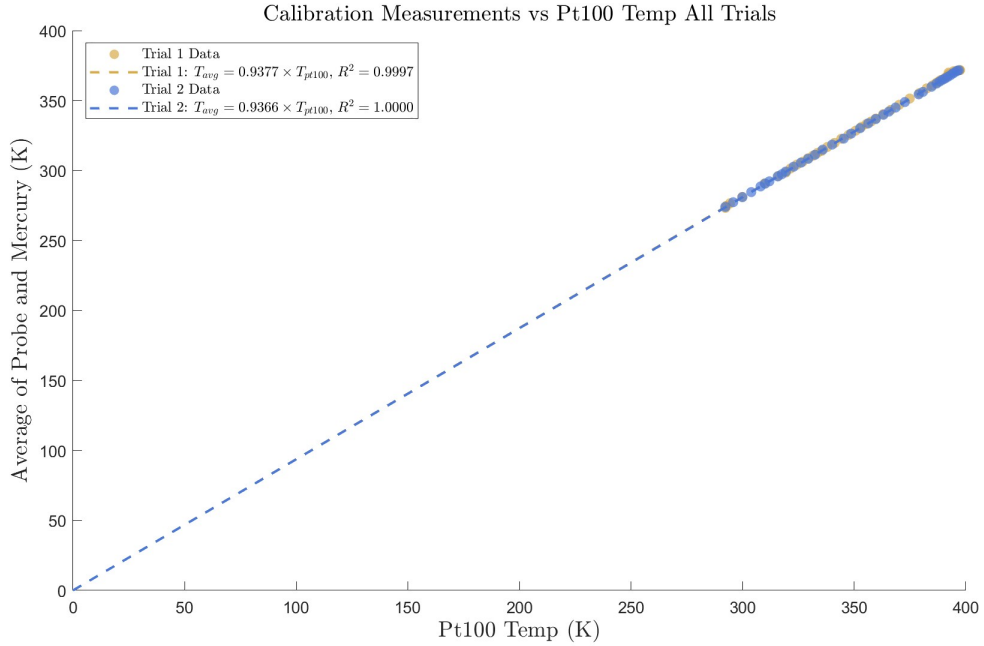


Figure A.5: Pt100 calibration data against Hg and digital thermometers.

A.4 Timing Calculations

To supplement the boundary cases (1.5 and 5.5 GPM) shown in Section 2.4, Figures A.6-A.8 present timing diagrams for the intermediate flow conditions of 2.5, 3.5, and 4.5 GPM. These diagrams follow the same structure as Figure 11, showing the loop travel time (gray bar), the high-speed imaging window (blue bar), and the 250 ms delay for imaging onset. All cases demonstrate that image capture (gold bar) occurs well within the first pass of the injected air, confirming that bubble measurements are free from recirculation effects and reflect true first-pass aeration dynamics.

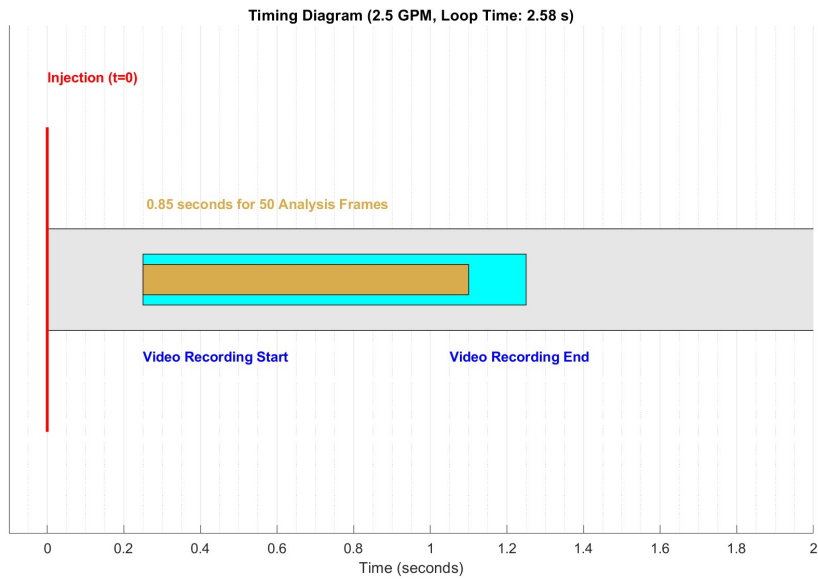


Figure A.6: Image timing diagram for 2.5 GPM trials.

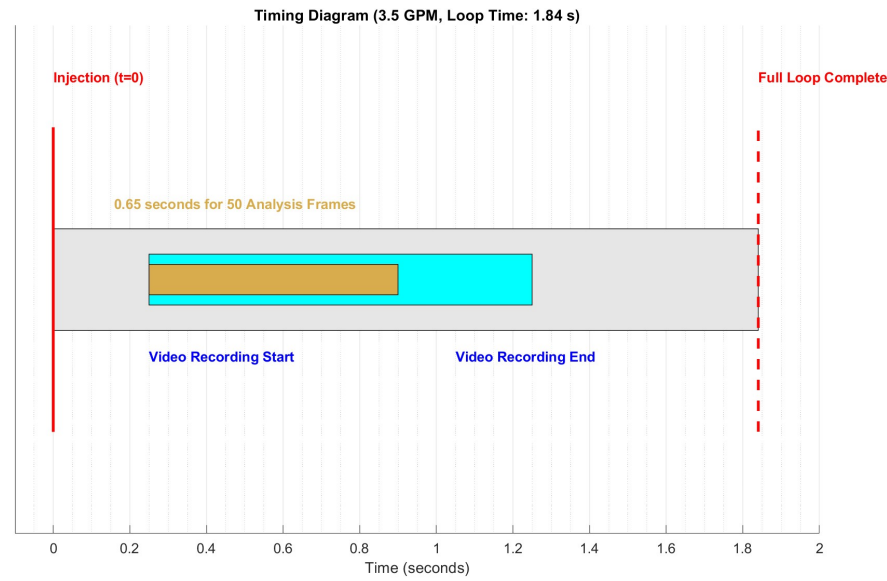


Figure A.7: Image timing diagram for 3.5 GPM trials.

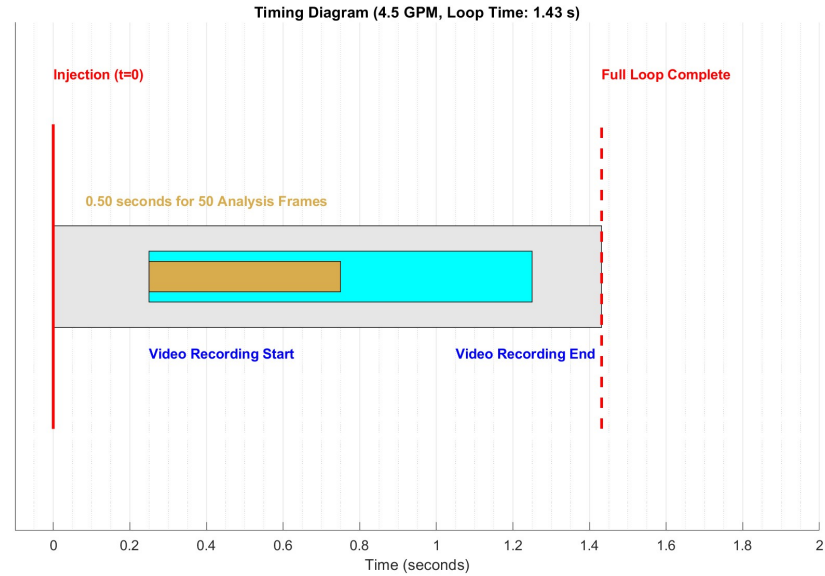


Figure A.8: Image timing diagram for 4.5 GPM trials.

A.5 Imaging Depth of Field

To quantify the depth of field (DOF) of the imaging system, the camera and lens setup described in Section 2.3 was positioned at its minimum focal distance and angled at approximately 35° relative to a precision ruler with 10-micron marker spacing. This setup is shown in Figure A.9a.

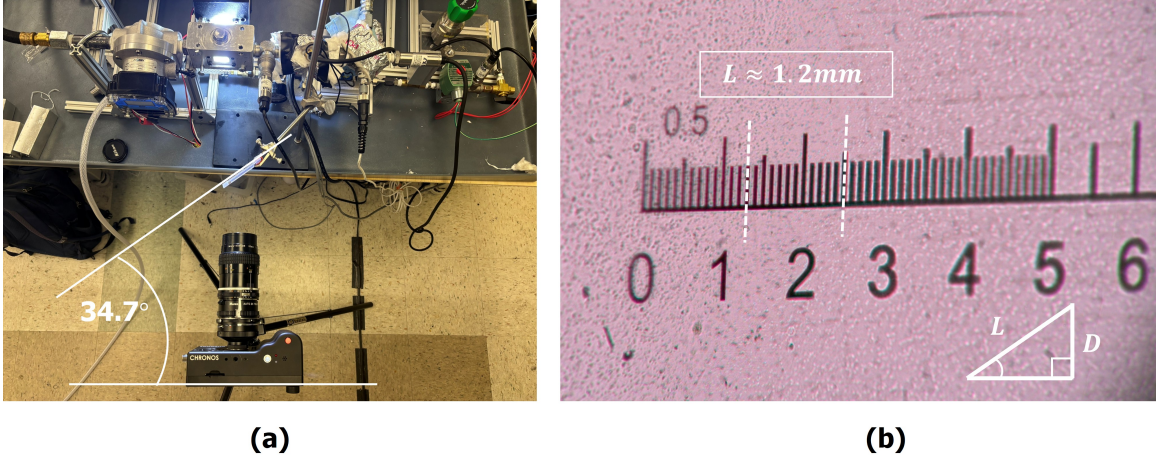


Figure A.9: Camera setup for depth of field measurement.

The number of sharply resolved rule markers visible in the recorded image was manually counted (Figure A.9b) and denoted as the total measured length (L) along the ruler. Because the ruler is inclined at 34.7° , the actual depth of field (D) is related to L via the following equation:

$$D = 1.2 \text{ mm} \cdot \sin(34.7) = 0.68 \text{ mm} \quad (\text{A.4})$$

This method offers a direct and reproducible means of measuring DOF under experimental imaging conditions.

A.6 Speed of Sound in Two-Phase Medium

Speed of sound calculations were made to ensure that the facility was operating in the subsonic regime and that bubbles are fragmented with the expected shear-driven mechanism. The speed of sound (c) of the two-phase flow at the throat is estimated by Equation A.5 (Nomura et al., 2011):

$$c = \sqrt{\frac{p}{\rho_l \alpha (1 - \alpha)}} \quad (\text{A.5})$$

Where p is fluid pressure, ρ_l is liquid density, and α is the air void fraction. For the most conservative estimate, the 5.5 GPM, 225°F, 0.5% aeration case ($\alpha = 0.005$) was used.

Pressure in the throat is estimated using the measured pressure downstream of the Venturi for the given flow rate and temperature combination, approximately 10.5 psi (72395 Pa). Density is calculated as described in Section 1.3 to be 880.6 kg/m^3 . This yields a speed of sound of approximately 128 m/s in the two-phase medium at the throat, much greater than the 12.3 m/s , so no compressibility effects or alternative breakup mechanisms must be considered at this time.

A.7 Operational Safety

All experiments in this study were conducted with careful consideration for personnel and equipment safety. The working fluid used was XIAMETER PMX-200 Silicone Fluid, 50 cSt, a clear, colorless, and low-volatility polydimethylsiloxane (PDMS). According to the manufacturer's Technical Data Sheet (DowChemicalCompany, 2024), the fluid has a high open-cup flash point of 318°C (604°F), well above the maximum experimental temperature of 225°F (107°C) used in this work. The open-cup flash point is applicable, as the facility's reservoir tank is maintained at ambient pressure and allows for ventilation of any generated fumes.

To ensure safe and even heating, the system employs a low-wattage immersion heater, minimizing localized overheating. An operator is physically present at all times, and the system is equipped with a dedicated emergency stop (E-stop) button that immediately cuts off power to both the heater and DC motor. A fire extinguisher is dedicated exclusively to this facility, ensuring immediate availability in case of emergency.

The pump motor includes a 10 A fuse which trips automatically in the event of excessive pressure or excessive flow, preventing damage to the system or escalation of unsafe conditions. Before any experimentation, new components are leak-tested at elevated temperature and pressure conditions to verify mechanical integrity.

Appendix B

Supplementary Plots and Data

B.1 Effect of Flow Rate Supplementary Plots

The following section provides supplementary plots to those provided in Section 3.3. Figures B.1 and B.2 show the data for the 7-degree and 30-degree diverging half angle nozzles respectively. The same trend of reduced d_{30} and σ_{LN} for increased flow rate is visible across all temperatures and angles.

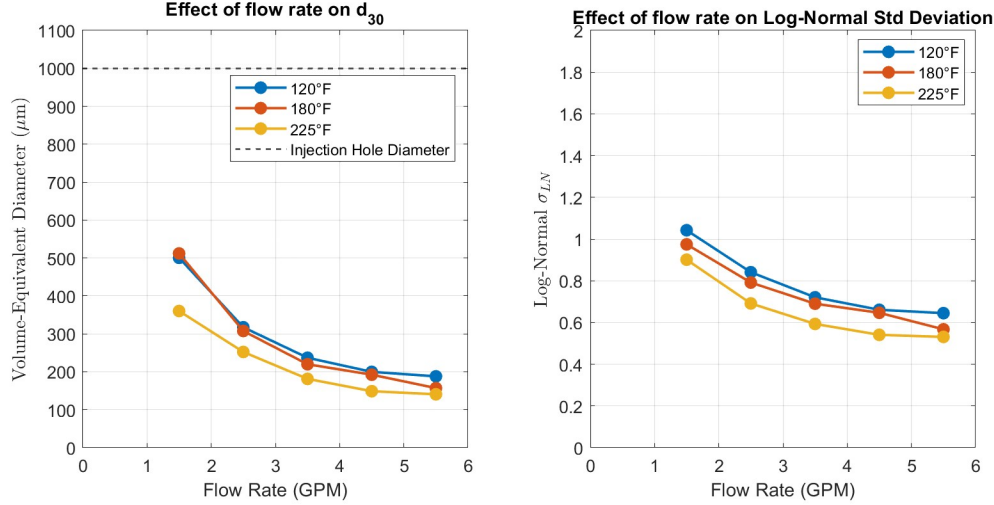


Figure B.1: Effect of flow rate on bubble diameter, $\beta = 7^\circ$, $\alpha = 0, 2\%$

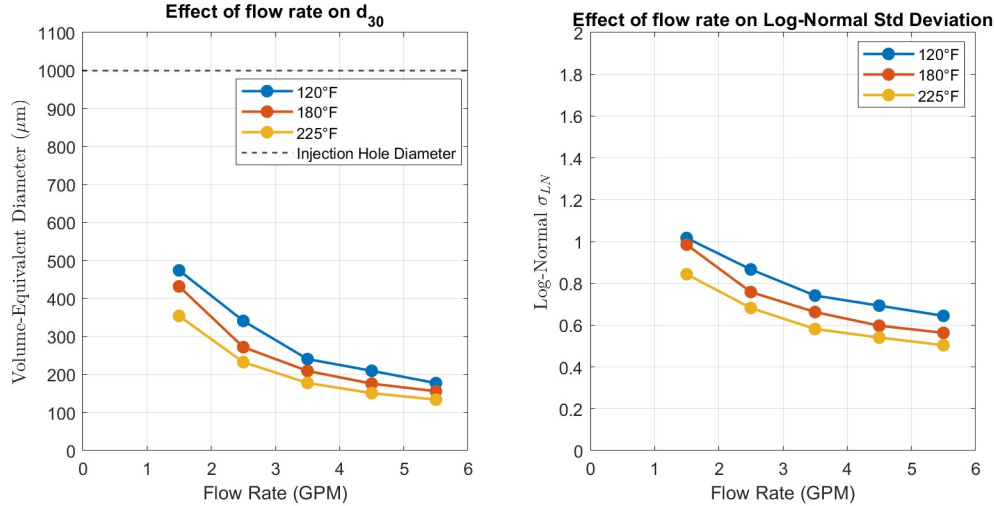


Figure B.2: Effect of flow rate on bubble diameter, $\beta = 30^\circ$, $\alpha = 0, 2\%$

B.2 Effect of Diverging Angle Supplementary Plots

The following section provides supplementary plots to those provided in Section 3.4. Figures B.3-B.6 show the diameter data for the 1.5-4.5 GPM trials. As discussed in Section 3.4, the trend of better 15° nozzle performance is only discernible at higher flow rates.

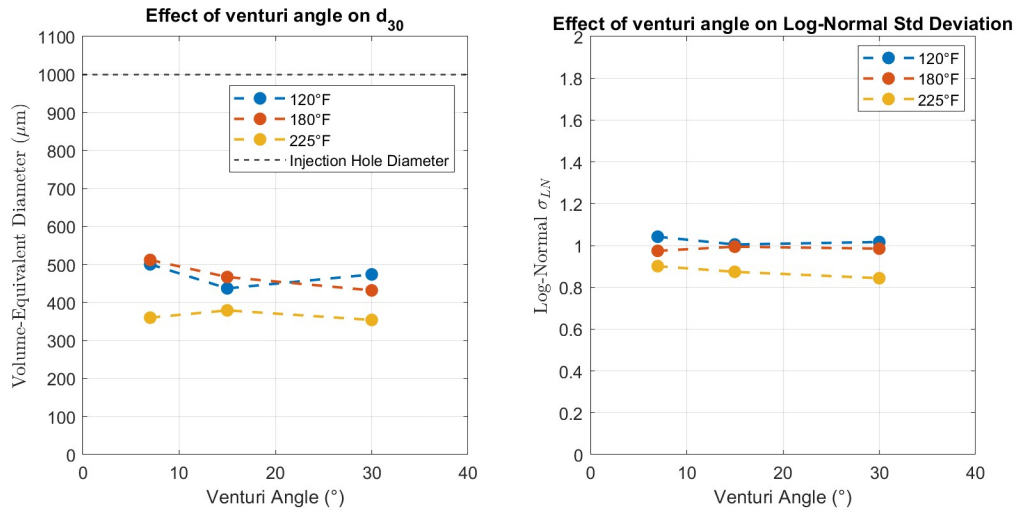


Figure B.3: Effect of Venturi angle β on bubble characteristics at 1.5 GPM, $\alpha = 0.2\%$

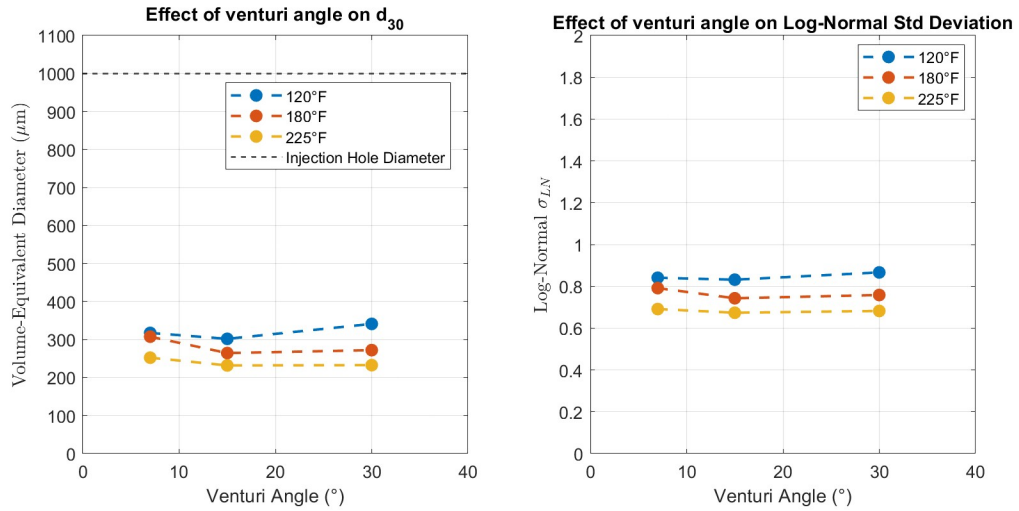


Figure B.4: Effect of Venturi angle β on bubble characteristics at 2.5 GPM, $\alpha = 0.2\%$

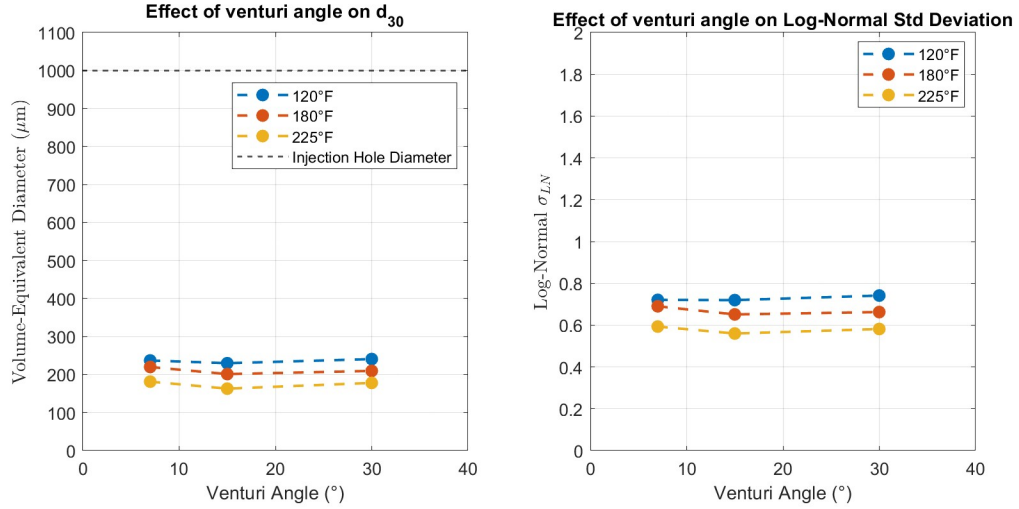


Figure B.5: Effect of Venturi angle β on bubble characteristics at 3.5 GPM, $\alpha = 0.2\%$

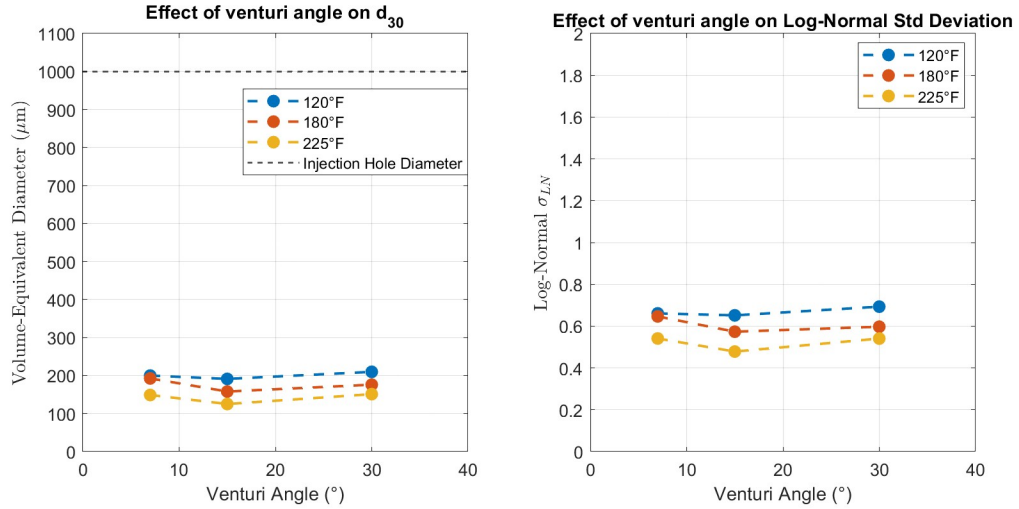


Figure B.6: Effect of Venturi angle β on bubble characteristics at 4.5 GPM, $\alpha = 0.2\%$

B.3 Effect of Temperature Supplementary Plots

The following section provides supplementary plots to that provided in Section 3.5. Figures B.7 and B.8 show the data for the 7-degree and 30-degree diverging half angle nozzles respectively. As discussed in Section 3.5, increased temperature (reduced viscosity and surface tension) appears to reduce bubble size and spread across all all flow rates. Data for the 1.5 GPM trial is presented with a dashed line, as the trend does not hold as consistently.

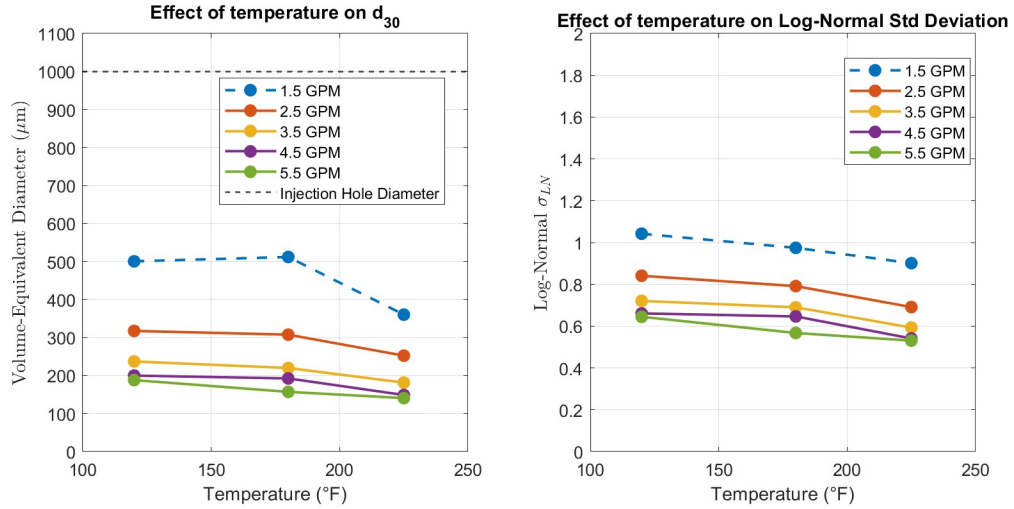


Figure B.7: Effect of temperature on bubble characteristics, $\beta = 7^\circ$, $\alpha = 0.2\%$

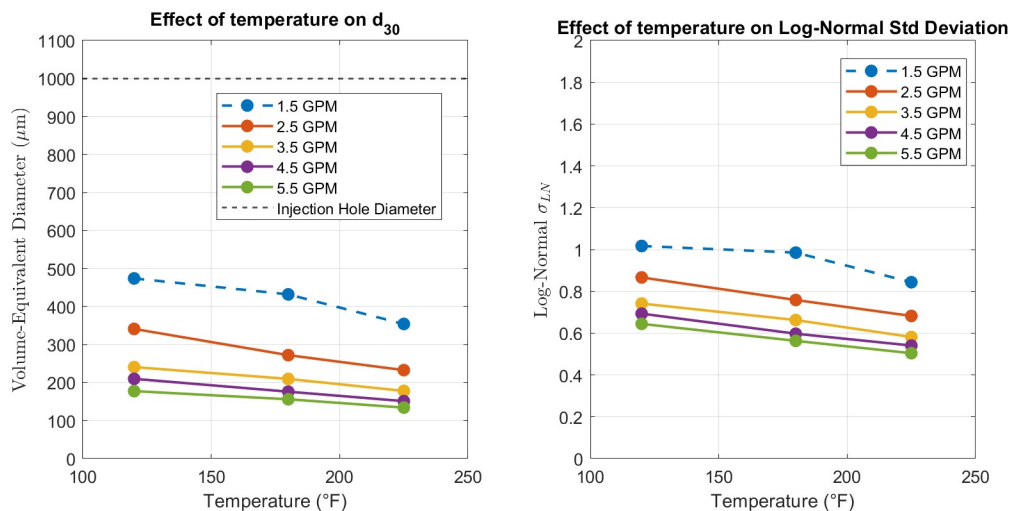


Figure B.8: Effect of temperature on bubble characteristics, $\beta = 30^\circ$, $\alpha = 0.2\%$